This is a repository copy of *Tuning hardness in calcite by incorporation of amino acids*.

White Rose Research Online URL for this paper:
http://eprints.whiterose.ac.uk/97761/

Version: Accepted Version

Article:
Kim, Y.Y., Carloni, J.D., Demarchi, B. et al. (12 more authors) (2016) Tuning hardness in calcite by incorporation of amino acids. Nature Materials, 15 (8). pp. 903-910. ISSN 1476-1122

https://doi.org/10.1038/nmat4631

Reuse
Unless indicated otherwise, fulltext items are protected by copyright with all rights reserved. The copyright exception in section 29 of the Copyright, Designs and Patents Act 1988 allows the making of a single copy solely for the purpose of non-commercial research or private study within the limits of fair dealing. The publisher or other rights-holder may allow further reproduction and re-use of this version - refer to the White Rose Research Online record for this item. Where records identify the publisher as the copyright holder, users can verify any specific terms of use on the publisher's website.

Takedown
If you consider content in White Rose Research Online to be in breach of UK law, please notify us by emailing eprints@whiterose.ac.uk including the URL of the record and the reason for the withdrawal request.

eprints@whiterose.ac.uk
https://eprints.whiterose.ac.uk/

Title: Tuning hardness in calcite by incorporation of amino acids

Authors:

Yi-Yeoun Kim[1]*, Joseph D. Carloni[2], Beatrice Demarchi[3], David Sparks[4], David G. Reid[5], Miki E. Kunitake[2], Chiu C. Tang[6], Melinda J. Duer[5], Colin L. Freeman[4], Boaz Pokroy[7], Kirsty Penkman[3], John H. Harding[4], Lara A. Estroff[2,8], Shefford P. Baker[2]* and Fiona C. Meldrum[1]*

Affiliations:

[1]School of Chemistry, University of Leeds, Woodhouse Lane, Leeds, LS2 9JT, UK.

[2]Department of Materials Science and Engineering, Cornell University, 329 Bard Hall, Ithaca, NY 14853, USA

[3]BioArCh, Departments of Chemistry and Archaeology, University of York, York, YO10 5DD, UK

[4]Department of Materials Science and Engineering, University of Sheffield, Mappin Street, Sheffield, S1 3JD, UK

[5]Department of Chemistry, University of Cambridge, Lensfield Road, Cambridge, CB2 1EW, UK

[6]Diamond Light Source, Harwell Science and Innovation Campus, Didcot, OX11 0DE, UK.

[7]Department of Materials Science and Engineering and the Russell Berrie Nanotechnology Institute, Technion Israel Institute of Technology Haifa 32000, Israel

[8]Kavli Institute at Cornell for Nanoscale Science, Ithaca, NY, USA

*Correspondence to: f.meldrum@leeds.ac.uk (FCM), shefford.baker@cornell.edu (SPB) or y.y.kim@leeds.ac.uk (YYK).

Structural biominerals are inorganic/organic composites that exhibit remarkable mechanical properties. However, the structure-property relationships of even the simplest building unit - mineral single crystals containing embedded macromolecules - remain poorly understood. Here, by means of a model biomineral made from calcite single crystals containing glycine (0-7 mol%) or aspartic acid (0-4 mol%), we elucidate the origin of the superior hardness of biogenic calcite. We analyzed lattice distortions in these model crystals by using x-ray diffraction and molecular dynamics simulations, and by means of solid-state nuclear magnetic resonance show that the amino acids are incorporated as individual molecules. We also demonstrate that nanoindentation hardness increased with amino acid content, reaching values equivalent to their biogenic counterparts. A dislocation pinning model reveals that the enhanced hardness is determined by the force required to cut covalent bonds in the molecules.

Biominerals such as bones, teeth and seashells are characterized by properties optimized for their functions. Despite being formed from brittle minerals and flexible polymers, nature demonstrates that it is possible to generate materials with strengths and toughnesses appropriate for structural applications[1]. At one level, the mechanical properties of these hierarchically structured materials are modelled as classical composites consisting of a mineral phase embedded in an organic matrix[2]. However, the single crystal mineral building blocks of biominerals are also composites[3], containing both aggregates of biomacromolecules as large as 20 nm[4,5] and inorganic impurities[6,7]. While it should be entirely possible to employ this simple biogenic strategy in materials synthesis[8,9], the strengthening and toughening mechanisms that result from these inclusions are still poorly understood[10,11]. This work addresses this challenge by analyzing hardening mechanisms in a simple model biomineral system: calcite single crystals containing known amounts of amino acids. We report synthetic calcite crystals with hardnesses equivalent to those of their biogenic counterparts, and offer a detailed explanation for the observed hardening.

Since plastic deformation in single crystals occurs by the motion of dislocations, hardness is enhanced by features that inhibit dislocation motion. The mechanisms by which guest species may harden ionic single crystals generally fall into two categories. Second phase particles directly block dislocation motion, requiring a dislocation to either cut through (shear) a particle or bypass it by a diffusive process to keep going[12]. Solutes (point defects) do not directly block dislocation motion, but the stress fields of the dislocations interact with those associated with misfitting solutes, retarding dislocation motion[12]. Biominerals, notably calcite, often deform plastically by twinning[11], but since twins grow by motion of "twinning dislocations"[13], these concepts also broadly apply to twin formation. To fully understand the hardening mechanisms of single crystal biominerals, one must determine the relationship between the hardness and the

concentrations of the different types of guest species. For example, the effect of Mg^{2+} substitutions was shown to be consistent with solute strengthening[14]. Determination of the hardening mechanism of occluded organic additives has proven far more challenging. While species ranging from small molecules[15,16] to peptides[17], proteins[18,19], nanoparticles[9,20,21] and fibers[22,23], have been incorporated in calcite, the effect of these inclusions on mechanical properties is not yet known. Occlusion of 200 nm latex particles within calcite single crystals was shown to reduce their hardness[8], while the incorporation of polymeric micelles having sizes comparable to those of the protein occlusions in biominerals was shown to increase hardness[9]. However, due to an inability to control the number of micelles occluded, it was not possible to quantitatively characterize their hardening effect.

The present study describes a model system – created by the incorporation of the amino acids aspartic acid (Asp) and glycine (Gly) within calcite – in which we can precisely *tune* the compositions of our single crystal composites over a wide range, and thus finally determine the origin of the hardening effects of small organic molecules. By application of x-ray diffraction and molecular dynamics simulations to characterize the local and global distortions of the crystal lattice, ssNMR to demonstrate that the amino acids are present as individual species within the crystal, nano-indentation to determine the hardness, and a dislocation pinning model, we show that the enhanced hardness is determined by the force required to cut a single covalent bond. This analysis provides strong evidence that the occluded molecules function more like second-phase particles than as point defects.

Incorporation of Asp and Gly in calcite single crystals

Calcite was precipitated in the presence of Asp or Gly using the ammonium diffusion method[24], and the crystals were characterized using SEM and optical microscopy (Fig. 1 and

Supplementary Figs. 1-3). Crystals were 20-50 μm in size and for both additives took the form of perfect rhombohedra at low additive concentrations, and at higher concentrations became elongated particles with highly roughened sides, which were capped at each apex with three, smooth {104} faces[25]. Aspartic acid has a stronger effect on calcite morphologies than glycine, as expected based on its charge under the crystallization conditions, such that equivalent morphologies are observed at much higher solution concentrations of Gly than Asp (eg. 100 -200 mM Gly as compared with 10-20 mM Asp).

The amounts of amino acids occluded within these crystals were determined using reverse-phase high-pressure liquid chromatography (rp-HPLC) after dissolution of the crystals. All samples were bleached before dissolution to remove surface-bound amino acids[26,27]. The relationship between the initial concentration of amino acids (AA) in the reaction solution ($[AA]_{Sol}$) and the mole fraction of amino acids incorporated ($[AA]_{Inc}$) was determined by holding $[Ca^{2+}]$ = 10 mM whilst varying the amino acid concentration (Fig. 2a). Looking first at Asp, there is a roughly linear relationship between $[Asp]_{Sol}$ and $[Asp]_{Inc}$ until $[Asp]_{Sol}$ = 50 mM and $[Asp]_{Inc}$ = 3.9 mol%, after which point $[Asp]_{Inc}$ reduces. This reduction in incorporation reflects a change in the particle structure from single crystal to polycrystalline, such that polycrystalline particles were excluded from further investigations. The incorporation of Gly shows a similar strong correlation with $[Gly]_{Sol}$, but is less efficient, with lower occlusion levels observed for equivalent values of $[AA]_{Sol}$ ($[Gly]_{Inc}$ = 1.1 mol% at 50 mM Gly). However, while Asp occlusion reaches a maximum at ≈ 3.9 mol%, Gly occlusion continues to increase, reaching values as high as 6.9 mol% at 400 mM Gly. These values are far higher than those obtained in a previous study of amino acid incorporation in calcite[15], highlighting the importance of the growth conditions in achieving occlusion. Higher Gly concentrations were not examined due to strong growth inhibition under those conditions.

A measure of the efficiency of amino acid occlusion was also obtained from the distribution coefficient, $D = [AA]_{inc}/[AA]_{sol}$, where the high values of D at low solution concentrations of Asp emphasize the far more efficient occlusion of Asp than Gly (Fig. 2b). This trend can be attributed to the charge on the Asp molecule, and its greater hydrophilicity[28,29]. The effect of the growth rate on amino acid occlusion was also investigated for Asp by precipitating calcite at $[Ca^{2+}]$ = 2–100 mM at a fixed initial $[Asp]_{Sol}$ = 10 mM (Figs. 2c and 2d and Supplementary Fig. 2). Incorporation was strongly dependent on the growth rate, increasing from 0.4 mol% at $[Ca^{2+}]$ = 2 mM to 1.9 mol% at $[Ca^{2+}]$ = 50 mM (Fig. 2c). This effect is additionally seen in the increase of D with crystal growth rate and $[Ca^{2+}]$ (Fig. 2d).

This observed increase in incorporation with increasing supersaturation is fully consistent with current understanding of additive interactions with growing crystals. AFM studies have clearly shown that small molecules (including Asp)[28] and ions including Mg^{2+} and SO_4^{2-} can selectively bind to either acute or obtuse step edges of calcite, [6,30-33] where this interaction then translates into their incorporation within the crystal lattice. This analysis is supported by a recent study which used *in situ* AFM to directly study the incorporation of 20 nm block copolymer micelles within calcite crystals following their binding to step edges.[34] The increase in density of step edges and kink sites that occurs with increasing supersaturation[30,34] therefore gives rise to higher additive occlusion levels.

Effects of incorporated amino acids on the lattice structure

Previous studies utilizing synchrotron high-resolution powder diffraction (PXRD) have shown that occlusion of organic molecules in both biogenic and synthetic calcium carbonates give rise to lattice distortions[3,15]. In the present study, the effects of the occluded amino acid on the crystal lattice were studied using synchrotron PXRD and the diffraction patterns were

modelled using full pattern analysis by Rietveld refinement as well as by line profile analysis. Occlusion of both Asp and Gly resulted in anisotropic lattice expansion, where the lattice distortions were about an order of magnitude greater along the *c*-axis than the *a*-axis (Figs. 3a and 3b). Both amino acids caused similar degrees of distortion along the *c*-axis at low incorporation levels, while the lattice distortions in Gly are higher than those in Asp at values of $[AA]_{Inc}$ exceeding 1 mol%, reaching 0.3 % at $[Asp]_{inc}$ = 3.9 mol% and 0.5 % at $[Gly]_{inc}$ = 6.9 mol%. Gly again caused somewhat more distortion along the *a*-axis at higher levels of occlusion.

Analysis of the peak broadening of the full spectra and individual PXRD peaks showed that the domain sizes fall in the ranges 200 to >1000 nm (Asp/calcite) and 500 to >1000 nm (Gly/calcite) (Supplementary Fig. 4). The degree of broadening (FWHM and/or integral breadth) varied across the different lattice planes, being greatest for the (006) planes, and in common with the lattice distortions, Gly had a greater effect than Asp at equivalent values of $[AA]_{Inc}$ (Figs. 3c and 3d). The broadening generally increased with increasing $[Asp]_{Inc}$, before levelling-off above 1 mol% occlusion, while for many of the lattice planes $[Gly]_{Inc}$ reached a maximum at ≈ 2-4 mol%, before decreasing again. (Figs. 3c and 3d, and Supplementary Fig. 5) This trend was particularly clear for the (006) planes. The consequence of this behaviour is that all of the diffraction peaks from the crystals occluding 6.9 mol% Gly have comparable broadening levels (Fig. 3d). It is also notable that the greatest peak broadening occurs at the same value of $[Gly]_{inc}$ at which the lattice distortions begin to saturate.

Occlusion of individual amino acids within calcite gives rise to inhomogeneous strains throughout the lattice, which increase the average lattice parameters. This observation is consistent with a model in which, as $[AA]_{inc}$ increases, the strain fields around the molecules begin to overlap, and the strain inhomogeneity decreases as the lattice distortions continue to

increase (Figs. 3e and 3f). Our data raise the possibility that the Gly molecules may be sufficiently close to each other at the higher occlusion levels that the local strain fields around them begin to overlap.

Solid state NMR (ssNMR) analysis of calcite crystals incorporating Asp

ssNMR was employed to determine whether the amino acids are isolated, or clustered within the calcite lattice. Looking first at the Asp/calcite system, crystals were precipitated in the presence of 25 mM of both 1,4-$^{13}C_2$ Asp and 3-^{13}C Asp at highest levels of incorporation (3.9 mol%), and were analyzed using proton driven spin diffusion (PDSD) (Fig. 4). The figures show conventional contour plots from the 2D PDSD experiment (in black), overlaid by a row (red) extracted from the dataset at the chemical shift of the Asp 3-C signal (Fig. 4a) and the overlapped Asp 1-C and Asp 4-C signals (Fig. 4b). The extracted rows reveal whether there is any spin diffusion between the two isotopomeric amino acids, which would indicate proximities of ≈ 0.5 nm between the Asp 3-C and the Asp 1-C and Asp 4-C. These would manifest as peak intensity in each of the extracted rows at the frequency corresponding to that of the "off diagonal" signal; the relevant frequencies are indicated by vertical red dashed lines in both figures. There is no intensity at either frequency, and thus no evidence of any intermolecular Asp-Asp association. Identical analyses were also performed for calcite precipitated in the presence of 1-^{13}C Gly and 2-^{13}C Gly, and the data again showed that the Gly molecules are individually dispersed in the lattice (Supplementary Fig. 6).

Simulations of the incorporation of Asp and Gly in calcite

Molecular dynamics simulations were performed to gain an understanding of the atomistic interactions between the mineral and amino acids. The calcite model consisted of a

block of calcite (34x44x34 $Å^3$) with 864 $CaCO_3$ formula units and two charge states of each amino acid (Asp^{2-}, Asp^{1-}, Gly^{1-} and Gly^0) were considered as the pKa values of the amino acids were close to experimental pH values (Supplementary Fig. 7). The amino acids were inserted by first removing Ca^{2+} and CO_3^{2-} ions, and then placing the amino acids within the resulting defect. Charge matching and minimum strains were achieved when each Gly^0 replaced one $CaCO_3$ formula unit, each Asp^{2-} replaced one $CaCO_3$ unit and a CO_3^{2-} ion, two Gly^{1-} replaced one $CaCO_3$ unit and a CO_3^{2-} ion, and two Asp^{1-} replaced two $CaCO_3$ units and a CO_3^{2-} ion.

The configurations of the Asp^{2-} and Gly^0 molecules in the calcite lattice are shown in Fig. 5a. The Asp molecules are occluded such that the carboxylic acid groups on Asp replace CO_3^{2-} groups on adjacent carbonate planes with a very good fit. A less favourable fit is obtained with Gly^0. This effect is also seen in the radial distribution data of the Ca-Ca distances in pure calcite and those for calcite occluding Asp^{2-} and Gly^0, which show that Gly^0 is more disruptive of the calcite lattice than Asp^{2-} (Fig. 5b). These distortions may well account for the reduced efficiency of incorporation of Gly than Asp. The binding configuration of the molecules is dominated by the requirements of the electrostatics of the lattice, where the carbonyl groups must replace the carbonate ions at the relevant lattice sites. Any contribution from hydrogen bonding is minor and does not affect the incorporation behaviour of these amino acids in calcite.

Simulations were also performed to model the lattice distortions arising from occlusion of amino acid molecules, where these data provide a bridge between our model of amino acid incorporation in the lattice and the experimental PXRD data. This model was implemented by expanding the crystal axes independently. The calculated configurational energies rose much faster when the crystal was strained along the *a*-axis than the *c*-axis (Fig. 5c), as is consistent with the elastic anisotropy of calcite[35]. For crystals containing 2.3 mol% Asp^{2-} and 2.8 mol% Gly^0 (to correspond to samples characterized by PXRD) the minimum energies are found at

lattice distortions that are in excellent agreement with the experimental values. The total inclusion energy also steadily increases with the amount of occluded amino acid (Fig. 5d), as would be expected based on a certain misfit per molecule.

Interestingly, the total inclusion energies (reported per mole of $CaCO_3$) were similar for both Asp^{2-} and Gly^0. Back-of the-envelope calculations of the misfits of Gly^0 and Asp^{2-} in the calcite lattice give values of 8.1 % for Gly^0 and 3.9 % for Asp^{2-} (see Supplementary note 1 for calculation), where these misfits result in large tensile strains in the calcite lattice in the neighbourhood of each AA molecule that drop off rapidly with distance from the molecule[36]. Although each occluded Gly is associated with larger strains than Asp, Gly is also significantly smaller than Asp, such that each molecule affects a smaller volume of the calcite lattice. Our data suggest that these contrasting effects are of similar magnitude here, giving rise to the similar inclusion energies.

Determination of the mechanical properties

Finally, the mechanical properties of the amino acid-containing calcite crystals were measured using nanoindentation. Indentations approximately 200 nm deep and 1.4 µm wide were made using a Berkovich (triangular pyramid) indenter, and the load-displacement data from each indentation were analyzed to determine hardness, H, and indentation modulus, E_{IT}[37]. Loads applied were sufficiently small (10 mN) that cracking was suppressed and indentations were formed by plastic deformation (Fig. 6a inset). In performing these experiments, it is noted that twin formation can occur during nanoindentation of single crystal calcite provided that indentation is executed along orientations where twinning is geometrically favorable[10,38], or if internal interfaces that can accommodate the enormous strains associated with twinning are present[11] or created by fracture[10,11]. None of our indentations were made in twin-compatible

orientations and no evidence of cracking or twin formation in either the load-displacement data or the surface topography was obtained. A more extensive discussion of twinning is provided in Supplementary note 5.

The hardness of the calcite crystals significantly increased with occluded amino acid content, starting at 2.5 GPa—equivalent to Iceland spar, a pure and highly perfect geologic form of calcite[10]—and reaching values of 4.1 ± 0.3 GPa for occlusion of 2.2 mol% Asp, and 4.1 ± 0.3 GPa for occlusion of 6.9 mol% Gly (Fig. 6a). Crystals with higher mol% of Asp inclusion were not tested due to the small sizes and irregular morphologies of these samples (Supplementary Fig. 1). These values are comparable to biogenic calcite (values of 3.4–4.2 GPa have been reported on the {001} face of the mollusc *Atrina rigida*)[10], and exceed the hardnesses of other synthetic calcite systems with occluded species reported to date, including calcite grown with occluded polymer micelles ($H_{max} \approx 3.0$ GPa)[9], and with Mg substitutions for Ca ($H_{max} \approx 3.4$ GPa)[14]. In contrast, the indentation modulus was insensitive to $[AA]_{inc}$, as expected based on a rule of mixtures model for a material containing a small volume fraction of a different phase.

Origin of hardening effect of occluded amino acids

Precipitation of $CaCO_3$ in the presence of Asp and Gly provides a system in which we can precisely tune the amounts of these small molecules within calcite single crystals across a broad composition range, allowing us to study in detail the relationship between the quantities of molecules occluded, their effects on the lattice distortions, and ultimately on the hardness. Since the calcite deformed plastically without cracking in these small-scale experiments (Fig. 6a inset), the origin of the hardening effect can be determined by considering the slip systems in the material (including both glide and twin systems) and the stresses needed to activate them with respect to the amount of amino acid occluded (see Supplementary note 2 for full derivations).

As hardness provides a measure of the resistance to motion of dislocations on these slip planes, the increase in hardness with increasing AA content demonstrates that the AA molecules provide effective impediments to dislocation motion.

The AA molecules can impede dislocations when either the stress fields around the molecules interact with the stress fields of the dislocations (like solutes), and/or when dislocations are blocked by the molecules themselves (like second phase particles). However, while the peak width (inhomogeneous strains) level off or decrease above $[AA]_{inc} \approx 1$ mol%, hardness continues to increase with $[AA]_{inc}$ occlusion (compare Figs. 3c and 3d with Fig. 6a, and see Supplementary note 3 for detailed explanations). Furthermore, the hardness is the same for both amino acids at the same $[AA]_{inc}$, despite the fact that the distortions are very different. These observations suggest that direct blocking by the molecules is the dominant hardening mechanism. To test this idea, we consider a dislocation interacting with a random array of AA molecules (Fig. 6b). The molecules impede the dislocation's motion, causing it to bow out[39]. Since lattice diffusion is not observed in calcite at room temperature, the dislocation can continue to move only by shearing the molecules. At each molecule, the dislocation line tension T is balanced by the resisting force of the molecule (Fig. 6c). When a critical force, known as the "cutting force" F_c, is reached, the dislocation cuts the molecule and moves on. Thus, if blocking by AA molecules dominates the increase in hardness, then F_c corresponds to the force required to cut a molecule.

If we assume that $T > F_c$, and that the hardness of the crystal is just the sum of its intrinsic resistance to dislocation motion—*i.e.* the hardness of pure calcite—and the additional hardening due to AA molecules, we can write (see Supplementary note 2 for derivation):

$$H = H_0 + 4.8(F_c / bL)\sqrt{F_c / 2T} \qquad (1)$$

Where H_o is the hardness of pure calcite, b the Burgers vector magnitude, and L the spacing between molecules. Since we know H_o, can estimate T and b, and have measured H as a function of $[AA]_{inc}$, if we can determine L from $[AA]_{inc}$, then we can determine the actual cutting force for the molecules. To estimate L, we consider the AA molecules to be uniformly distributed throughout the crystal, which is consistent with the ssNMR data, and approximate the configuration of the molecules as a square array. This analysis gives $L = (C_{v,AA}t)^{-0.5}$ where $C_{v,AA}$ is the number of AA molecules/volume and t is the thickness of a thin slice, which is set equal to the diameter of the AA molecule (see Supplementary note 4 for derivation). We can now use Equation (1) to find the cutting force, F_c, for each experimentally measured H, where we obtain values around 1 nN (Fig. 6d). This value lies just below reported strengths of single covalent bonds (1.5 to 4 nN)[40-42] and well above a typical ionic bond strength of 0.1 nN[43]. Since the hardness represents an average of all of the events that inhibit dislocation motion, this result strongly suggests that the hardening effect of these occluded molecules comes from the force required to shear them.

Further support for this model comes from the functional form of the variation of hardness with $[AA]_{inc}$. For a constant obstacle strength (F_c in this case), H should vary linearly with the inverse of the obstacle spacing, L^{-1} (Equation (1)). Since $L = (C_{v,AA}t)^{-0.5}$, H is expected to vary linearly with $(C_{v,AA}t)^{0.5}$. A power law fit to the H *vs.* $C_{v,AA}t$ data returns an exponent of 0.52, so H indeed varies linearly with $(C_{v,AA}t)^{0.5}$ (Fig. 6e). Despite the different sizes of the molecules, when intermolecular spacings are taken into account, the hardness depends on the bond strengths in the individual molecules, which are essentially the same for Asp and Gly.

Outlook

This work provides new insights into the mechanical properties of inorganic/ organic nanocomposites. By creating a system that is at first sight very simple – the occlusion of amino acids within calcite single crystals – we are finally able to quantitatively correlate the composition of the resultant composite crystals to the hardness. At the heart of our strategy is the ability to achieve extremely high levels of occlusion of up to 3.9 mol% Asp and 6.9 mol% Gly, while retaining calcite single crystals. Analysis of the changes in hardness and lattice distortions with respect to the composition shows that the hardening effect derives primarily from dislocations cutting the amino acids, as indicated by the fact that the estimated dislocation obstacle cutting force is in good agreement with the strength of the covalent bonds in the amino acid backbones. With the ability to tune the composition and hardness of calcite crystals, our nanocomposite system also opens the door to in-depth characterization of deformation mechanisms using transmission electron microscopy (TEM), which would provide further understanding of the possible role of twinning during deformation. These results are of particular significance to the mechanical properties of single crystal biominerals, and open up the possibility of using this strategy to tailor the mechanical properties of a wide range of materials.

References

1 Wegst, U. G. K., Bai, H., Saiz, E., Tomsia, A. P. & Ritchie, R. O. Bioinspired structural materials. *Nat. Mater.* **14**, 23-36 (2015).

2 Fratzl, P. & Weinkamer, R. Nature's hierarchical materials. *Prog. Mater. Sci.* **52**, 1263-1334 (2007).

3 Weber, E. & Pokroy, B. Intracrystalline inclusions within single crystalline hosts: from biomineralization to bio-inspired crystal growth. *CrystEngComm* **17**, 5873-5883 (2015).

4 Gries, K., Kroger, R., Kubel, C., Fritz, M. & Rosenauer, A. Investigations of voids in the aragonite platelets of nacre. *Acta Biomater.* **5**, 3038-3044 (2009).

5 Li, H. Y. *et al.* Calcite prisms from mollusk shells (atrina rigida): swiss-cheese-like organic–inorganic single-crystal composites. *Adv. Funct. Mater.* **21**, 2028-2034 (2011).

6 Davis, K. J., Dove, P. M. & De Yoreo, J. J. The role of Mg2+ as an impurity in calcite growth. *Science* **290**, 1134-1137 (2000).

7 Stephenson, A. E. *et al.* Peptides enhance magnesium signature in calcite: insights into origins of vital effects. *Science* **322**, 724-727 (2008).

8 Kim, Y. Y. *et al.* Bio-inspired synthesis and mechanical properties of calcite-polymer particle composites. *Adv. Mater.* **22**, 2082-2086 (2010).

9 Kim, Y. Y. *et al.* An artificial biomineral formed by incorporation of copolymer micelles in calcite crystals. *Nat. Mater.* **10**, 890-896 (2011).

10 Kunitake, M. E., Mangano, L. M., Peloquin, J. M., Baker, S. P. & Estroff, L. A. Evaluation of strengthening mechanisms in calcite single crystals from mollusk shells. *Acta Biomater.* **9**, 5353-5359 (2013).

11 Li, L. & Ortiz, C. Pervasive nanoscale deformation twinning as a catalyst for efficient energy dissipation in a bioceramic armour. *Nat. Mater.* **13**, 501-507 (2014).

12 Courtney, T. H. *Mechanical behavior of materials*. 2nd ed. edn, (Waveland Press, Long Grove 2005).

13 Christian, J. W. & Mahajan, S. Deformation Twinning. *Prog. Mater. Sci.* **39**, 1-157 (1995).

14 Kunitake, M. E., Baker, S. P. & Estroff, L. A. The effect of magnesium substitution on the hardness of synthetic and biogenic calcite. *MRS Commun.* **2**, 113-116 (2012).

15 Borukhin, S. *et al.* Screening the incorporation of amino acids into an inorganic crystalline host: the case of calcite. *Adv. Funct. Mater.* **22**, 4216-4224 (2012).

16 Magnabosco, G. *et al.* Calcite single crystals as hosts for atomic-scale entrapment and slow release of drugs. *Adv. Healthcare Mater.* **4**, 1510-1516 (2015).

17 Metzler, R. A., Tribello, G. A., Parrinello, M. & Gilbert, P. Asprich peptides are occluded in calcite and permanently disorder biomineral crystals. *J. Am. Chem. Soc.* **132**, 11585-11591 (2010).

18 Albeck, S., Aizenberg, J., Addadi, L. & Weiner, S. Interactions of various skeletal intracrystalline components with calcite crystals. *J. Am. Chem. Soc.* **115**, 11691-11697 (1993).

19 Aizenberg, J., Hanson, J., Koetzle, T. F., Weiner, S. & Addadi, L. Control of macromolecule distribution within synthetic and biogenic single calcite crystals. *J. Am. Chem. Soc.* **119**, 881-886 (1997).

20 Kulak, A. N. *et al.* One-pot synthesis of an inorganic heterostructure: uniform occlusion of magnetite nanoparticles within calcite single crystals. *Chem. Sci.* **5**, 738-743 (2014).

21 Kulak, A. N., Yang, P. C., Kim, Y. Y., Armes, S. P. & Meldrum, F. C. Colouring crystals with inorganic nanoparticles. *Chem. Commun.* **50**, 67-69 (2014).
22 Li, H., Xin, H. L., Muller, D. A. & Estroff, L. A. Visualizing the 3D internal structure of calcite single crystals grown in agarose hydrogels. *Science* **326**, 1244-1247 (2009).
23 Li, H. Y. & Estroff, L. A. Calcite growth in hydrogels: assessing the mechanism of polymer-network incorporation into single crystals. *Adv. Mater.* **21**, 470-473 (2009).
24 Ihli, J., Bots, P., Kulak, A., Benning, L. G. & Meldrum, F. C. Elucidating mechanisms of diffusion-based calcium carbonate synthesis leads to controlled mesocrystal formation. *Adv. Funct. Mater.* **23**, 1965-1973 (2013).
25 Chen, C. L., Qi, J. H., Tao, J. H., Zuckermann, R. N. & DeYoreo, J. J. Tuning calcite morphology and growth acceleration by a rational design of highly stable protein-mimetics. *Sci. Rep.* **4**, 6266 (2014).
26 Penkman, K. E. H., Kaufman, D. S., Maddy, D. & Collins, M. J. Closed-system behaviour of the intra-crystalline fraction of amino acids in mollusc shells. *Quat. Geochronol* **3**, 2-25 (2008).
27 Tomiak, P. J. *et al.* Testing the limitations of artificial protein degradation kinetics using known-age massive Porites coral skeletons. *Quat Geochronol* **16**, 87-109 (2013).
28 Elhadj, S., De Yoreo, J. J., Hoyer, J. R. & Dove, P. M. Role of molecular charge and hydrophilicity in regulating the kinetics of crystal growth. *Proc. Natl. Acad. Sci. U. S. A.* **103**, 19237-19242 (2006).
29 Hopp, T. P. & Woods, K. R. Prediction of protein antigenic determinants from amino acid sequences. *Proc. Natl. Acad. Sci. U. S. A.* **78**, 3824-3828 (1981).
30 De Yoreo, J. J. *et al.* Rethinking classical crystal growth models through molecular scale insights: consequences of kink-limited Kinetics. *Cryst. Growth Des.* **9**, 5135-5144 (2009).
31 Nielsen, L. C., De Yoreo, J. J. & DePaolo, D. J. General model for calcite growth kinetics in the presence of impurity ions. *Geochim. Cosmochim. Acta* **115**, 100-114 (2013).
32 Paquette, J. & Reeder, R. J. Relationship between Surface-Structure, Growth-Mechanism, and Trace-Element Incorporation in Calcite. *Geochim. Cosmochim. Acta* **59**, 735-749 (1995).
33 Staudt, W. J., Reeder, R. J. & Schoonen, M. A. A. Surface structural controls on compositional oning of $So4^{2-}$ and $SeO4^{2-}$ in synthetic calcite single crystals. *Geochim. Cosmochim. Acta* **58**, 2087-2098 (1994).
34 Cho, K-R. *et al.* Direct observation of mineral-organic composite formation reveals occlusion mechanism. *Nat Commun* **7**, 10187 (2016).
35 Bass, J. D. in *Mineral Physics & Crystallography: A Handbook of Physical Constants* 45-63 (American Geophysical Union, 2013).
36 Eshelby, J. D. The determination of the elastic field of an ellipsoidal inclusion, and related problems. *Proc. R. Soc. London, Ser. A* **241**, 376-396 (1957).
37 Oliver, W. C. & Pharr, G. M. An improved technique for determining hardness and elastic-modulus using load and displacement sensing indentation experiments. *J. Mater. Res.* **7**, 1564-1583 (1992).
38 Clayton, J. D. & Knap, J. Phase field modeling of twinning in indentation of transparent crystals. *Modell. Simul. Mater. Sci. Eng.* **19**, 085005 (2011).
39 Foreman, A. J. E. & Makin, M. J. Dislocation movement through random arrays of obstacles. *Philos. Mag.* **14**, 911-924 (1966).

40 Akbulatov, S., Tian, Y. C. & Boulatov, R. Force-reactivity property of a single monomer is sufficient to predict the micromechanical behavior of its polymer. *J. Am. Chem. Soc.* **134**, 7620-7623 (2012).
41 Diesendruck, C. E. *et al.* Mechanically triggered heterolytic unzipping of a low-ceiling-temperature polymer. *Nat. Chem.* **6**, 624-629 (2014).
42 Grandbois, M., Beyer, M., Rief, M., Clausen-Schaumann, H. & Gaub, H. E. How strong is a covalent bond? *Science* **283**, 1727-1730 (1999).
43 Spruijt, E., van den Berg, S. A., Stuart, M. A. C. & van der Gucht, J. Direct measurement of the strength of single ionic bonds between hydrated charges. *ACS Nano* **6**, 5297-5303 (2012).

Acknowledgments: This work was supported by an Engineering and Physical Sciences Research Council (EPSRC) Leadership Fellowship (FCM and YYK, EP/H005374/1), by an EPSRC Materials World Network grant (EP/J018589/1, FCM and YYK) and an EPSRC Programme Grant (grant EP/I001514/1) which funds the Materials Interface with Biology (MIB) consortium (FCM, JH and DS). We acknowledge Diamond Light Source for time on beamline I11 under commissioning time and proposal EE10137. LAE, JDC, MEK, and SPB were supported by the US National Science Foundation (NSF) via a Materials World Network grant (DMR 1210304). BP acknowledges support from the European Research Council under the European Union's Seventh Framework Program (FP/2007–2013)/ERC Grant Agreement n° [336077]. BD and KP were supported by the Leverhulme Trust and the EU reintergration grant (PERG07-GA-2010-268429, FP7), project “mAARiTIME”. Ashely Coutu and Sheila Taylor are thanked for technical help for RP-HPLC analysis. This work made use of the Cornell Center for Materials Research Shared Facilities, which are supported through the NSF MRSEC program (DMR-1120296). The authors also thank Matthew Collins for his intellectual contribution to the development of the study and for helpful discussions throughout.

Author Contributions

Y.Y.K. led the experimental work, preparing samples and carrying out EM and XRD, and analysing the data; B.D. and K.P. performed HPLC measurements and analysed the occlusion data; J.D.C. and M.E.K. carried out nanoindentation measurements, J.D.C, S.P.B. and L.A.E. analysed and modelled mechanical data; S.P.B. and L.A.E. co-supervised J.D.C and M.E.K.; D.S. carried out molecular dynamic simulations work and C.L.F. and J.H.H. supervised DS and analysed simulation data; C.C.T. assisted with the XRD experiments; B.P. assisted with analysis and discussion of the XRD data; D.G.R. and M.J.D. performed the NMR studies and analyses; F.C.M. originated and supervised the project. All authors contributed to the preparation of the manuscript.

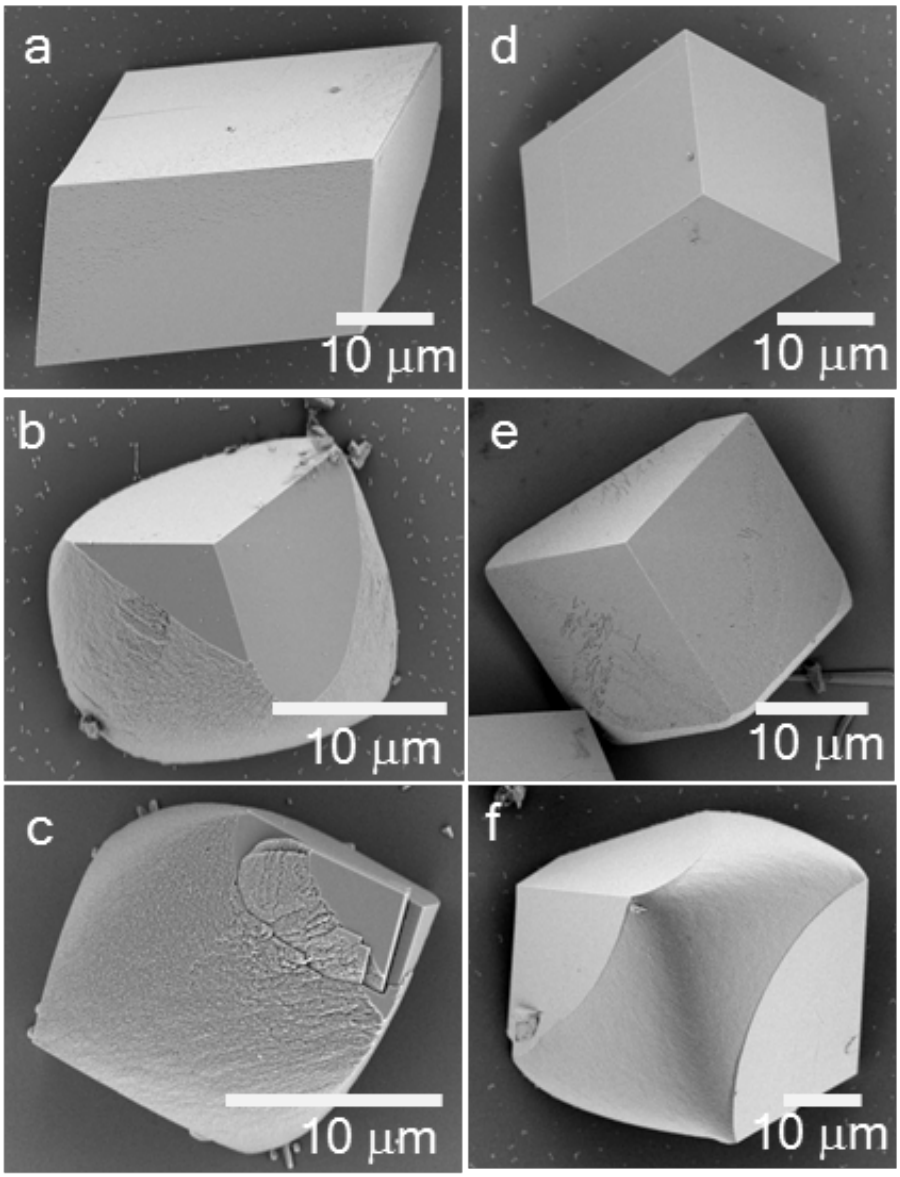

Figure 1. **Crystal morphologies.** Representative SEM images showing calcite crystals precipitated with different conditions of $[AA]_{sol}$ and initial $[Ca]_{sol}$ = 10 mM. (a to c) $[Asp]_{sol}$ = (a) 5 mM (b) 20 mM (c) 50 mM. (d to f) $[Gly]_{sol}$ = (d) 10 mM (e) 100 mM (f) 200 mM.

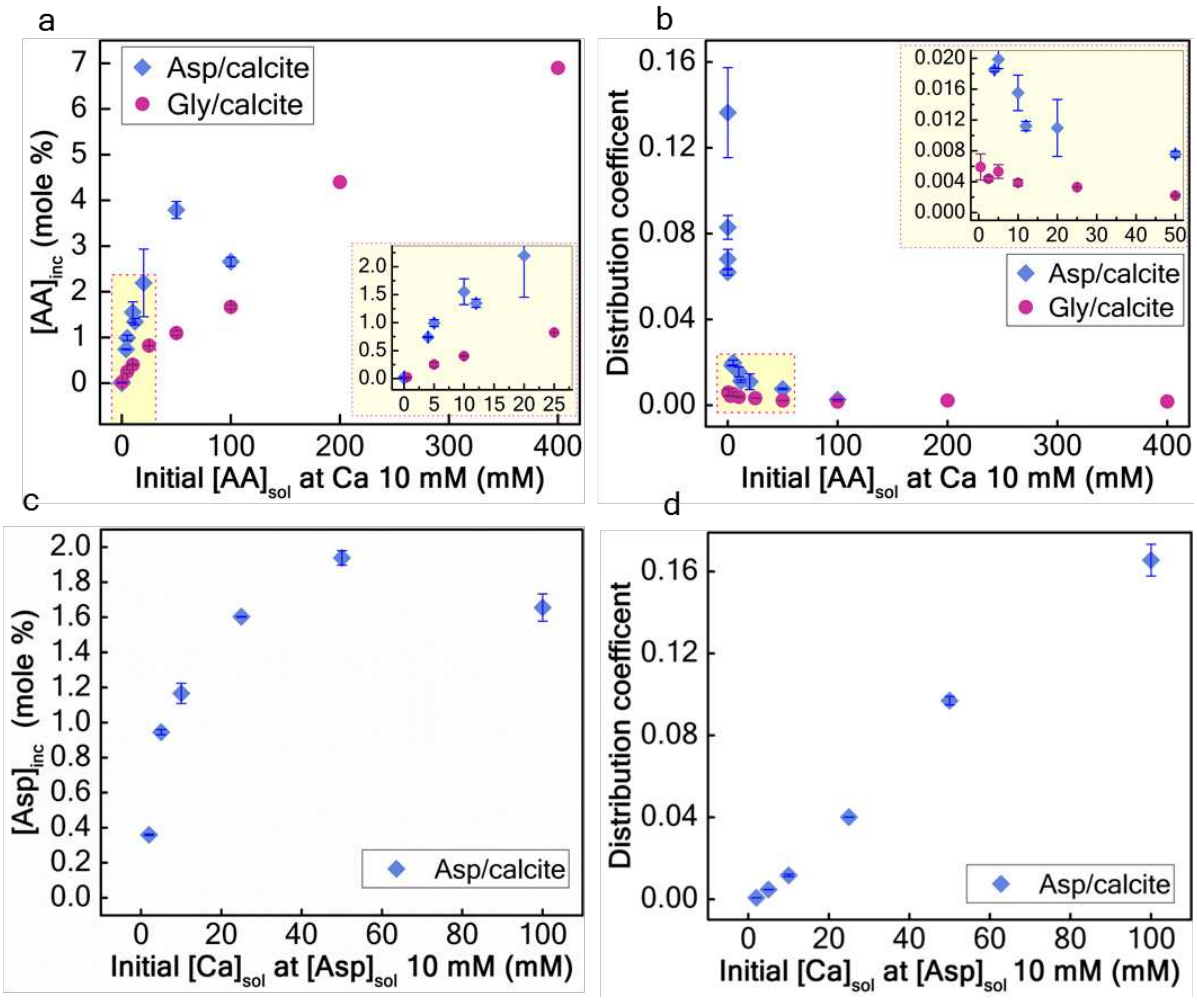

Figure 2. Occlusion of aspartic acid and glycine in calcite. (a) The amount of amino acid occluded within the $CaCO_3$ crystals, $[AA]_{inc}$, as a function of the initial concentration of amino acid in solution, $[AA]_{sol}$, for Asp and Gly at $[Ca^{2+}]_{sol}$ = 10 mM. (b) The distribution coefficients for Asp and Gly in calcite as a function of the initial $[AA]_{sol}$ at $[Ca^{2+}]$ = 10 mM. The insets show sub-section of the respective graphs. (c) The amount of Asp occluded as a function of $[Ca^{2+}]_{sol}$ at an initial $[Asp]_{sol}$ = 10 mM. (d) The distribution coefficient of Asp in calcite at and initial $[Asp]_{Sol}$ = 10 mM. The error bars shown are defined as s.d. for 3-5 measurements, and those for the Gly/calcite system were too small to show.

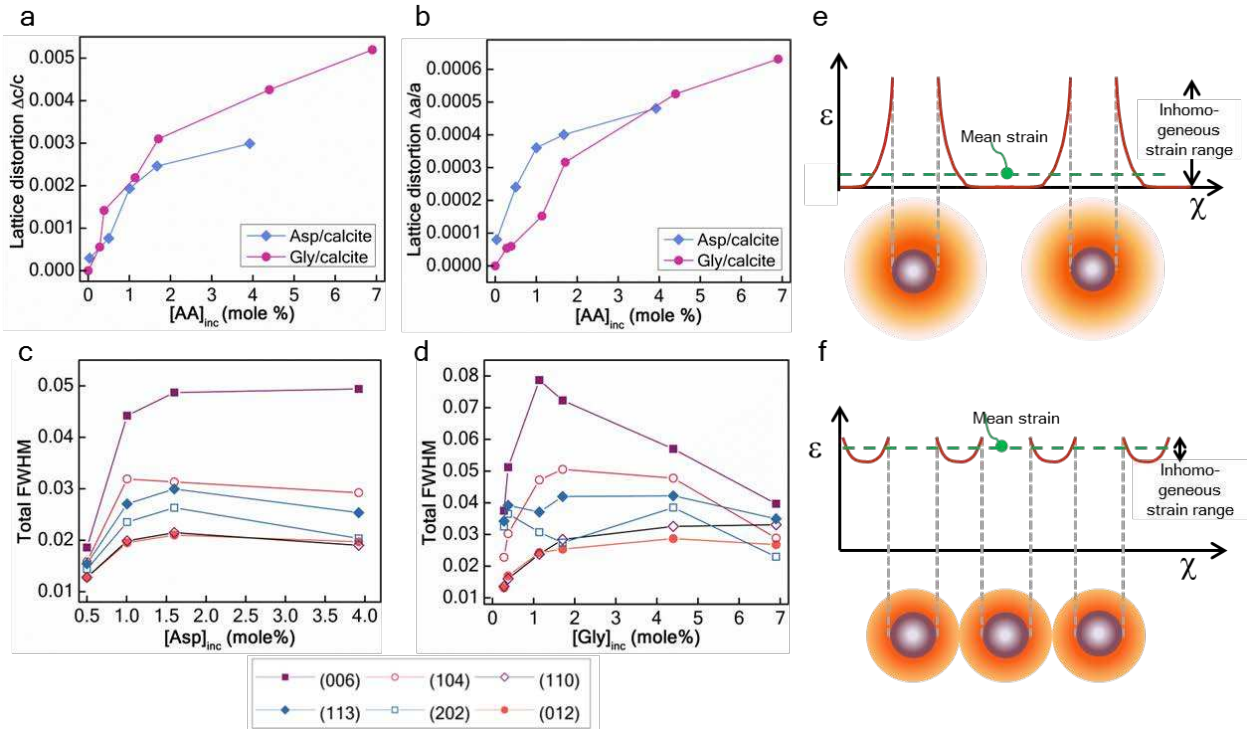

Figure 3. High resolution PXRD analysis. (a and b) Lattice distortions arising from the incorporation of Asp and Gly in calcite, (a) along the *c*-axis and (b) the *a*-axis. (c and d) XRD peak broadening (FWHM) due to inhomogeneous strains induced by (c) Asp and (d) Gly incorporation. The inhomogeneous strains show a maximum with (e) Asp (f) Gly while the lattice distortion continues to increase, as is consistent with overlapping of the strain fields associated with the individual molecules as the spacings between the molecules become smaller.

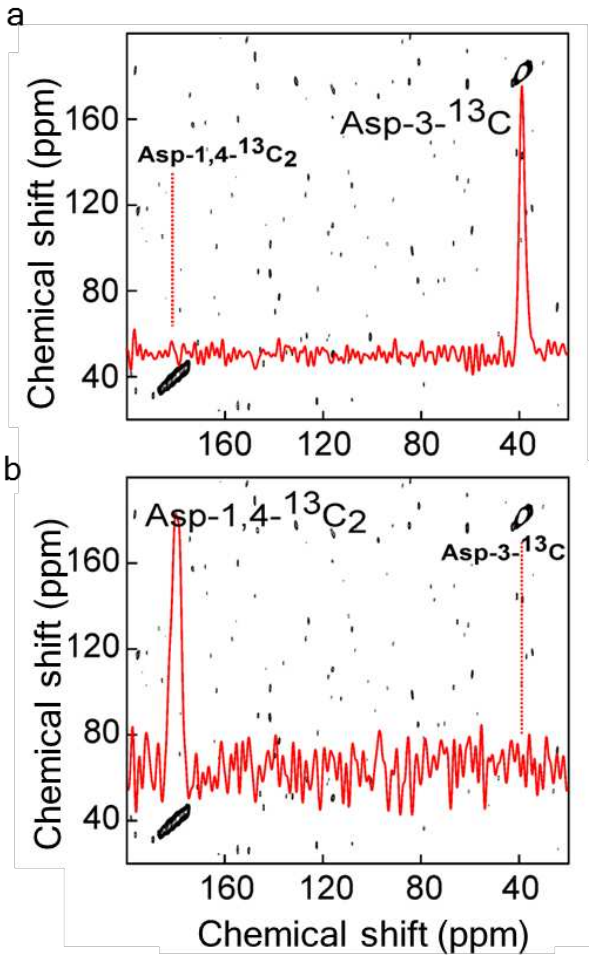

Figure 4. Solid state NMR analysis. Contour plots of a proton driven spin diffusion (PDSD) analysis of calcite precipitated in the presence of [1,4-$^{13}C_2$ Asp] = [3-^{13}C Asp] = 25 mM. The red traces are rows extracted from the 2D dataset at the frequency of the (a) 3-^{13}C signal and (b) the overlapped 1,4-^{13}C signals. Proximity between the 3-^{13}C and the 1,4-^{13}C labelled Asp would manifest as a peak (in the red trace) at the frequency of the (a) 1,4-^{13}C and (b) 3-^{13}C, as indicated by the dashed vertical red line.

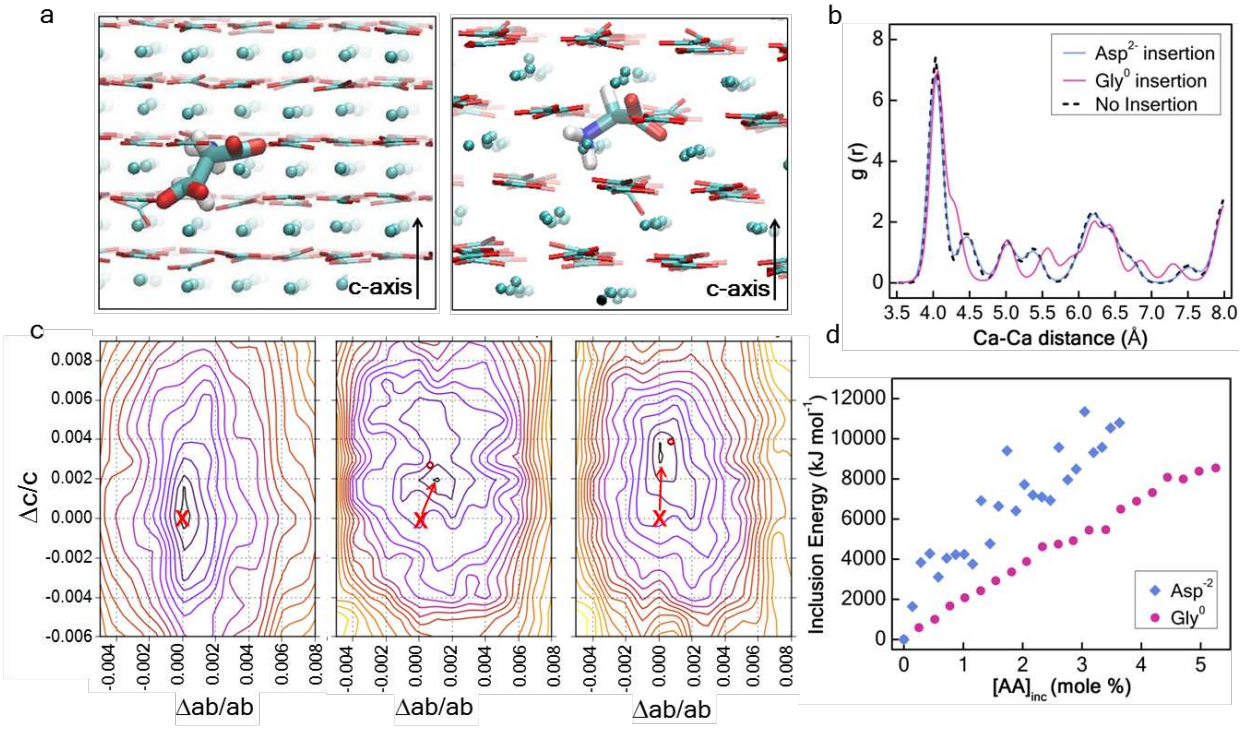

Figure 5. Molecular dynamics simulations. (a) Schematics showing Asp^{2-} and Gly^{0} occluded in the calcite crystal. (b) Radial distribution function of Ca-Ca distances in pure calcite and calcite with occluded Asp^{2-} and Gly^{0}. (c) Configurational energies of calcite with occluded Asp^{2-} and Gly^{o}, calculated on expansion of the calcite crystal along the *c*-axis and *a*-axis. The energy minima are found at Δc/c values of 0.002 and 0.003 for the incorporation of 2.3 mol% Asp^{2-} and 2.8 mol% Gly^{0} respectively. Red 'x' denotes the energy minimum of pure calcite, where the arrow shows the distortion from the pure calcite sample to the experimental values found at 'o'. (d) The total occlusion energy for Asp^{2-} and Gly^{0}.

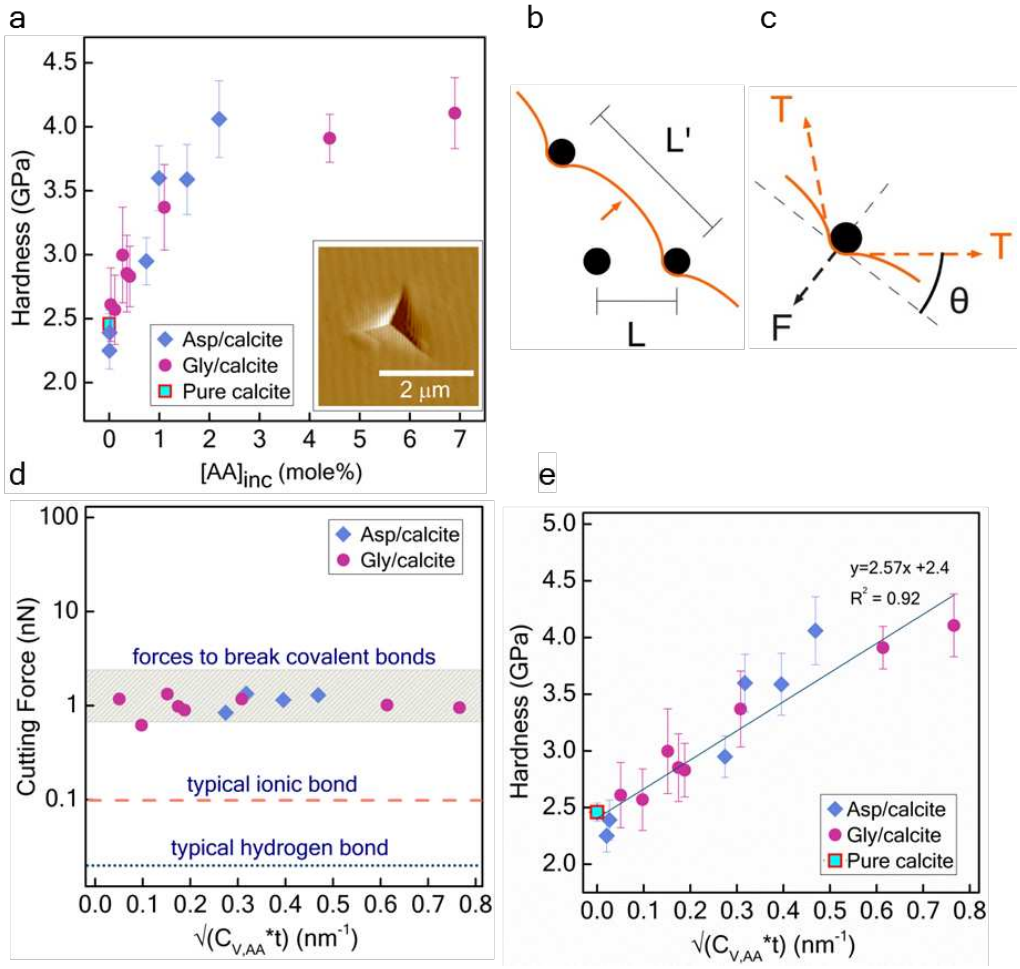

Figure 6. Mechanical properties. (a) Hardness *vs.*$[AA]_{inc}$ for calcite occluding Asp and Gly (inset: scanning force image of representative plastic indentation in calcite). Schematics of (b) dislocation bowing out between AA molecule pinning points, and (c) force balance between dislocation line tension T and the resisting force F provided by the molecule. The "cutting force" F_c is the force needed for the dislocation to cut the molecule. Since $F_c << T$, the effective spacing L' is greater than the actual spacing L. (d) F_c calculated using measured hardness and estimated molecular spacings as compared with expected mechanical bond strengths. (e) Hardness vs. $L^{-1} = (C_{v,AA}*t)^{0.5}$, where the linear behaviour supports blocking by molecules as the strengthening mechanism. The error bars shown are defined as s.d. and are the result of 28 measurements.

Methods

The materials used are listed in the Supplementary materials.

$CaCO_3$ precipitation. The two amino acids, Asp and Gly, were mixed with 2 – 100 mM aqueous solutions of $CaCl_2.2H_2O$ to give amino acid concentrations of 0.001 – 100 mM Asp and 0.1 - 400 mM Gly. 40 mL of the prepared solutions were transferred to plastic Petri dishes (90 mm) containing glass slides, which had previously been cleaned with Piranha solution (H_2SO_4 70 vol% H_2O_2 30 vol%), and $CaCO_3$ was precipitated using the ammonium carbonate diffusion method.[24] This was achieved by covering the Petri dishes with Parafilm pierced with multiple holes and placing them in a dessicator previously charged with 5 g of freshly crushed $(NH_4)_2CO_3$ powder. Crystallisation was then allowed to proceed for 2 days (unless otherwise stated), after which time the glass slides were removed from solution, washed thoroughly with Millipore water and ethanol, and oven-dried (40 ^oC) prior to further characterization.

$CaCO_3$ precipitation in the presence of 400 mM Gly took approximately 5-6 days; this was the maximum concentration of Gly employed. In the case of Asp, a mixture of single crystal and polycrystalline particles formed at Asp concentrations above 50 mM, and principally polycrystalline particles formed above 100 mM Asp (Supplementary Fig. 1). The maximum Asp concentration employed was therefore 50 mM. Investigation of the influence of the initial Ca concentration in solution showed that while higher initial Ca concentrations favor occlusion of the amino acids (Figs. 2c and 2d), they also drive the generation of polycrystalline calcite at lower Asp concentrations (Supplementary Fig. 2). For example, at an initial [Ca] = 25 mM, polycrystalline calcite was observed at 25 mM Asp (Supplementary Fig. 3). An initial [Ca] = 10 mM was therefore chosen as the standard condition as this offered efficient occlusion of the amino acids, while still retaining single crystallinity of calcite.

Calcite crystals were also precipitated in the presence of 13C-labelled Asp and Gly such that they could be analyzed in Proton driven spin diffusion (PDSD) experiments to determine the proximities of the occluded amino acids. Calcite/Asp crystals were precipitated from solutions of concentrations [Ca^{2+}] = 10 mM and [1,4-$^{13}C_2$ Asp] = [3-^{13}C Asp] = 25 mM, while calcite/Gly crystals were precipitated from solutions of [Ca^{2+}] = 10 mM and [1-^{13}C Gly] = [2-^{13}C Gly] = 100 mM.

Quantification of the incorporation of amino acids within calcite crystals. All calcite samples were bleached in 12% w/v sodium hypochlorite for 48 hrs before analysis using 50 µL of hypochlorite per mg of calcite. This effectively removes surface-bound amino acids, as demonstrated during the characterisation of biomolecules occluded within a range of biominerals[26,27,44] The amino acids were then extracted from the $CaCO_3$ crystals by dissolving them in cold 2 M HCl (using a minimum of 10 µL HCl per mg of calcite). The acid was then evaporated and the samples rehydrated with an adequate volume of a rehydration fluid containing 0.01 mM HCl, 0.77 mM sodium azide at pH 2, and an internal standard (0.01 mM L-homo-arginine). The rehydrated samples were analyzed for chiral amino acids on an automated reverse-phase high-performance liquid chromatography (RP-HPLC) system equipped with a fluorescence detector, using a modification of the method of Kaufman and Manley[45]. In brief, 2 µL of rehydrated sample was mixed online with 2.2 µL of derivatizing reagent (260 mM N-isobutyryl-l-cysteine, 170 mM o-phthaldialdehyde, in 1 M potassium borate buffer, adjusted to pH 10.4 with KOH) immediately before injection. This set-up is optimized for the routine separation of enantiomeric pairs, which is achieved on a C18 HyperSil BDS column using a gradient elution of sodium acetate buffer (pH 6.00 ± 0.01), methanol, and acetonitrile. Quantification of the amounts of Asp and Gly occluded within the calcite crystals was achieved

using calibration curves, as reported in[46] using the (normalized) RP-HPLC peak areas, taking into account the mass of the calcite sample analyzed and the volume of rehydration fluid used.

Characterization of amino acid/calcite composite particles. The crystals were analyzed using Scanning Electron Microscopy (SEM), optical microscopy, and selected samples were also analyzed using synchrotron X-ray powder diffraction. For SEM, particles on glass substrate were mounted on aluminum stubs using carbon sticky pads, and were coated with 5 nm Pt/Pd using FEI Nova NanoSEM.

Solid state nuclear magnetic resonance (ssNMR) spectroscopy analysis. All ssNMR spectra were recorded on a Bruker Avance I NMR spectrometer with a 9.4 T superconducting magnet, operating at 400 MHz for ^{1}H and 100 MHz for ^{13}C. Samples were packed into 4 mm zirconia rotors, with Teflon tape being used to fill out empty space within the rotor. Magic angle spinning (MAS) rate was 10 kHz. The standard cross polarization (CP) sequence in the Bruker pulse program library was used; ^{1}H 90° pulse length 2.5 μs, contact time 2.5 ms, with a ramped pulse on ^{1}H and spin lock field 70 kHz. During acquisition, spinal64 decoupling at 100 kHz RF field strength was applied on ^{1}H. Repetition time was 2 s between successive acquisitions to allow relaxation.

Proton driven spin diffusion (PDSD) experiments were conducted using the same initial cross polarization parameters as employed in the ^{13}C CP experiments. At 10 kHz MAS, the magnetization was allowed to evolve at single-quantum coherence during the incremental delay (t_1), and returned to zero quantum coherence by a ^{13}C 90° pulse of 3.8 μs. ^{1}H decoupling was switched off during this mixing period of 100 ms to allow transfer of ^{13}C magnetization via dipolar coupling and spin diffusion[47] with a ^{13}C 90° readout pulse at the end of the mixing

period. During both the incremental delay and acquisition periods, spinal64 decoupling was applied at 100 kHz. The pulse sequence used was an adapted version of the Avance I CP spin diffusion experiment in the Bruker library.

Synchrotron powder X-ray diffraction (PXRD) analysis. The high-resolution PXRD measurements were carried out on the synchrotron beamline (I11) at Diamond Light Source Ltd, Didcot, UK. Instrument calibration and wavelength refinement (λ=0.8257156(10) Å) were performed using high quality NIST silicon powder (SRM640c) and instrumental contribution to the peak widths does not exceed 0.004^{o48}. Diffractograms were recorded from the specimens at room temperature. Sample powders for analysis were loaded into 0.7 mm borosilicate glass capillaries, and to avoid intensity spikes from individual crystallites, the samples were rotated during measurements at a rate of 60 rps. PXRD data was then obtained using high-resolution MAC (multi-analyzer crystal) diffraction scans, with scan times of 1800 s.

The structural parameters were refined by Rietveld analysis using GSAS and PANalytical X'Pert HighScore Plus software. Lattice distortion, strain and size analysis was performed using both Rietveld analysis for whole spectrum and line profile analysis for the (012), (104), (001), (110) and (113) reflections using PANalytical X'Pert HighScore Plus software. Goodness of fitness values for all the analyzed samples are summarized in Supplementary Tables 1 and 2.

To analyze peak shape, peak broadening was expressed as FWHM and Integral Breadth. (Fig. 3 and Supplementary Figs 4 and 5) Total FWHM is the full width at half maximum for each of the peaks, while Integral Breadth is the width of a rectangle that can be placed within the peak that has the same area as the net peak area, (Net area/net height). Microstrain (%) is derived by line profile analysis and shows the microstrain contribution to the total line

broadening. Coherence length (nm) is derived by line profile analysis and shows the coherence length contribution to the total line broadening (Supplementary Fig. 4).

Mechanical testing. Cyanoacrylate resin was poured over glass slides supporting precipitated calcite/amino acid crystals and was then allowed to set overnight. The resin and crystals were polished using graded Al_2O_3 lapping films and a final 50 nm Al_2O_3 powder (Buehler micropolish γ–Al_2O_3) suspended in a water and 2-methyl-2,4-pentanediol mix (Green Lube, Allied High Tech) until the crystals were exposed for measurement (Supplementary Fig. 8). The surface roughness of samples produced following this protocol was less than 10 nm RMS as determined using the indenter tip as a scanning force probe.

Nanoindentation measurements were performed on exposed calcite/amino acid crystals with in-plane sizes of 20–60 µm using a Berkovich (≈120 nm tip radius) diamond indenter in a commercial nanoindenter system (Hysitron TriboIndenter 900). Before data collection, the shape of the tip was calibrated using the method of Oliver and Pharr[49]. Each indent consisted of five-second load, hold, and unload segments with a maximum load of 2500 µN, resulting in ≈200 nm deep indents. The unloading segment was used to calculate the indentation modulus and hardness[49]. The maximum load was chosen to create an indentation large enough to sample a homogeneous volume and minimize the effects of surface roughness, while allowing multiple indents per sample. Surface topography scans were performed with the indenter tip before and after indenting to ensure indentations were located at least 5 µm away from any edges.

The hardness and modulus of calcite depends on the orientation of the crystal with respect to the nanoindenter tip. For example, for indentations on the {001} facet of calcite, the hardness ranges from 2.3 to 2.5 GPa and the indentation modulus ranges from 68 to 77 GPa with azimuthal angle[10]. For randomly oriented crystals, averaging over multiple crystals with

multiple indentations provides an average hardness and modulus over a range of crystallographic orientations. In this work, 5 to 8 different randomly-oriented crystals were selected for each growth condition, and 4-10 indentations were made per crystal, resulting in at least 28 measurements for each amino acid concentration.

Supplementary Information

Tuning Hardness in Calcite by Incorporation of Amino Acids

Yi-Yeoun Kim[1]*, Joseph D. Carloni[2], Beatrice Demarchi[3], David Sparks[4], David G. Reid[5], Miki E. Kunitake[2], Chiu C. Tang[6], Melinda J. Duer[5], Colin L. Freeman[4], Boaz Pokroy[7], Kirsty Penkman[3], John H. Harding[4], Lara A. Estroff[2,8], Shefford P. Baker[2]* and Fiona C. Meldrum[1]*

Content:

- **Supplementary methods**
- **Supplementary notes 1-5**
- **Supplementary figures 1-9**
- **Supplementary tables 1-2**
- **Supplementary equations 1-5**
- **Supplementary references (*1-37)***

Supplementary Methods

Materials. $CaCl_2 \cdot 2H_2O$, $(NH_4)_2CO_3$, sodium L-aspartate and glycine were purchased from Sigma-Aldrich, while glycine (1-13C and 2-13C) and L-aspartic acid (3-13C and 1,4-13C 99%) were purchased from Cambridge Isotope Laboratories Inc. All chemicals were used without further purification.

$CaCO_3$ precipitation. The two amino acids, Asp and Gly, were mixed with 2 – 100 mM aqueous solutions of $CaCl_2.2H_2O$ to give amino acid concentrations of 0.001 – 100 mM Asp and 0.1 - 400 mM Gly. 40 mL of the prepared solutions were transferred to plastic Petri dishes (90 mm) containing glass slides, which had previously been cleaned with Piranha solution (H_2SO_4 70 vol% H_2O_2 30 vol%), and $CaCO_3$ was precipitated using the ammonium carbonate diffusion method.[1] This was achieved by covering the Petri dishes with Parafilm pierced with multiple holes and placing them in a dessicator previously charged with 5 g of freshly crushed $(NH_4)_2CO_3$ powder. Crystallisation was then allowed to proceed for 2 days (unless otherwise stated), after which time the glass slides were removed from solution, washed thoroughly with Millipore water and ethanol, and oven-dried (40 ^oC) prior to further characterization.

$CaCO_3$ precipitation in the presence of 400 mM Gly took approximately 5-6 days; this was the maximum concentration of Gly employed. In the case of Asp, a mixture of single crystal and polycrystalline particles formed at Asp concentrations above 50 mM, and principally polycrystalline particles formed above 100 mM Asp (Supplementary Fig. 1). The maximum Asp concentration employed was therefore 50 mM. Investigation of the influence of the initial Ca concentration in solution showed that while higher initial Ca concentrations favor occlusion of the amino acids (Figs. 2c and 2d), they also drive the generation of polycrystalline calcite at

lower Asp concentrations (Supplementary Fig. 2). For example, at an initial [Ca] = 25 mM, polycrystalline calcite was observed at 25 mM Asp (Supplementary Fig. 3). An initial [Ca] = 10 mM was therefore chosen as the standard condition as this offered efficient occlusion of the amino acids, while still retaining single crystallinity of calcite.

Calcite crystals were also precipitated in the presence of 13C-labelled Asp and Gly such that they could be analyzed in Proton driven spin diffusion (PDSD) experiments to determine the proximities of the occluded amino acids. Calcite/Asp crystals were precipitated from solutions of concentrations [Ca^{2+}] = 10 mM and [1,4-$^{13}C_2$ Asp] = [3-^{13}C Asp] = 25 mM, while calcite/Gly crystals were precipitated from solutions of [Ca^{2+}] = 10 mM and [1-^{13}C Gly] = [2-^{13}C Gly] = 100 mM.

Quantification of the incorporation of amino acids within calcite crystals. All calcite samples were bleached in 12% w/v sodium hypochlorite for 48 hrs before analysis using 50 µL of hypochlorite per mg of calcite. This effectively removes surface-bound amino acids, as demonstrated during the characterisation of biomolecules occluded within a range of biominerals[2-4] The amino acids were then extracted from the $CaCO_3$ crystals by dissolving them in cold 2 M HCl (using a minimum of 10 µL HCl per mg of calcite). The acid was then evaporated and the samples rehydrated with an adequate volume of a rehydration fluid containing 0.01 mM HCl, 0.77 mM sodium azide at pH 2, and an internal standard (0.01 mM L-homo-arginine). The rehydrated samples were analyzed for chiral amino acids on an automated reverse-phase high-performance liquid chromatography (RP-HPLC) system equipped with a fluorescence detector, using a modification of the method of Kaufman and Manley[5]. In brief, 2 µL of rehydrated sample was mixed online with 2.2 µL of derivatizing reagent (260 mM N-isobutyryl-l-cysteine, 170 mM o-phthaldialdehyde, in 1 M potassium borate buffer, adjusted to

pH 10.4 with KOH) immediately before injection. This set-up is optimized for the routine separation of enantiomeric pairs, which is achieved on a C18 HyperSil BDS column using a gradient elution of sodium acetate buffer (pH 6.00 ± 0.01), methanol, and acetonitrile. Quantification of the amounts of Asp and Gly occluded within the calcite crystals was achieved using calibration curves, as reported in[6] using the (normalized) RP-HPLC peak areas, taking into account the mass of the calcite sample analyzed and the volume of rehydration fluid used.

Characterization of amino acid/calcite composite particles. The crystals were analyzed using Scanning Electron Microscopy (SEM), optical microscopy, and selected samples were also analyzed using synchrotron X-ray powder diffraction. For SEM, particles on glass substrate were mounted on aluminum stubs using carbon sticky pads, and were coated with 5 nm Pt/Pd using FEI Nova NanoSEM.

Solid state nuclear magnetic resonance (ssNMR) spectroscopy analysis. All ssNMR spectra were recorded on a Bruker Avance I NMR spectrometer with a 9.4 T superconducting magnet, operating at 400 MHz for ^{1}H and 100 MHz for ^{13}C. Samples were packed into 4 mm zirconia rotors, with Teflon tape being used to fill out empty space within the rotor. Magic angle spinning (MAS) rate was 10 kHz. The standard cross polarization (CP) sequence in the Bruker pulse program library was used; ^{1}H 90° pulse length 2.5 μs, contact time 2.5 ms, with a ramped pulse on ^{1}H and spin lock field 70 kHz. During acquisition, spinal64 decoupling at 100 kHz RF field strength was applied on ^{1}H. Repetition time was 2 s between successive acquisitions to allow relaxation.

Proton driven spin diffusion (PDSD) experiments were conducted using the same initial cross polarization parameters as employed in the ^{13}C CP experiments. At 10 kHz MAS, the

magnetization was allowed to evolve at single-quantum coherence during the incremental delay (t_1), and returned to zero quantum coherence by a ^{13}C 90° pulse of 3.8 μs. ^{1}H decoupling was switched off during this mixing period of 100 ms to allow transfer of ^{13}C magnetization via dipolar coupling and spin diffusion[7] with a ^{13}C 90° readout pulse at the end of the mixing period. During both the incremental delay and acquisition periods, spinal64 decoupling was applied at 100 kHz. The pulse sequence used was an adapted version of the Avance I CP spin diffusion experiment in the Bruker library.

Synchrotron powder X-ray diffraction (PXRD) analysis. The high-resolution PXRD measurements were carried out on the synchrotron beamline (I11) at Diamond Light Source Ltd, Didcot, UK. Instrument calibration and wavelength refinement (λ=0.8257156(10) Å) were performed using high quality NIST silicon powder (SRM640c) and instrumental contribution to the peak widths does not exceed 0.004°[8]. Diffractograms were recorded from the specimens at room temperature. Sample powders for analysis were loaded into 0.7 mm borosilicate glass capillaries, and to avoid intensity spikes from individual crystallites, the samples were rotated during measurements at a rate of 60 rps. PXRD data was then obtained using high-resolution MAC (multi-analyser crystal) diffraction scans, with scan times of 1800 s.

The structural parameters were refined by Rietveld analysis using GSAS and PANalytical X'Pert HighScore Plus software. Lattice distortion, strain and size analysis was performed using both Rietveld analysis for whole spectrum and line profile analysis for the (012), (104), (001), (110) and (113) reflections using PANalytical X'Pert HighScore Plus software. Goodness of fitness values for all the analyzed samples are summarized in Supplementary Tables 1 and 2.

To analyze peak shape, peak broadening was expressed as FWHM and Integral Breadth. (Fig. 3 and Supplementary Figs 4 and 5) Total FWHM is the full width at half maximum for

each of the peaks, while Integral Breadth is the width of a rectangle that can be placed within the peak that has the same area as the net peak area, (Net area/net height). Microstrain (%) is derived by line profile analysis and shows the microstrain contribution to the total line broadening. Coherence length (nm) is derived by line profile analysis and shows the coherence length contribution to the total line broadening (Supplementary Fig. 4).

Mechanical testing. Cyanoacrylate resin was poured over glass slides supporting precipitated calcite/amino acid crystals and was then allowed to set overnight. The resin and crystals were polished using graded Al_2O_3 lapping films and a final 50 nm Al_2O_3 powder (Buehler micropolish γ–Al_2O_3) suspended in a water and 2-methyl-2,4-pentanediol mix (Green Lube, Allied High Tech) until the crystals were exposed for measurement (Supplementary Fig. 8). The surface roughness of samples produced following this protocol was less than 10 nm RMS as determined using the indenter tip as a scanning force probe.

Nanoindentation measurements were performed on exposed calcite/amino acid crystals with in-plane sizes of 20–60 µm using a Berkovich (≈120 nm tip radius) diamond indenter in a commercial nanoindenter system (Hysitron TriboIndenter 900). Before data collection, the shape of the tip was calibrated using the method of Oliver and Pharr[9]. Each indent consisted of five-second load, hold, and unload segments with a maximum load of 2500 µN, resulting in ≈200 nm deep indents. The unloading segment was used to calculate the indentation modulus and hardness[9]. The maximum load was chosen to create an indentation large enough to sample a homogeneous volume and minimize the effects of surface roughness, while allowing multiple indents per sample. Surface topography scans were performed with the indenter tip before and after indenting to ensure indentations were located at least 5 µm away from any edges.

The hardness and modulus of calcite depends on the orientation of the crystal with respect to the nanoindenter tip. For example, for indentations on the {001} facet of calcite, the hardness ranges from 2.3 to 2.5 GPa and the indentation modulus ranges from 68 to 77 GPa with azimuthal angle[10]. For randomly oriented crystals, averaging over multiple crystals with multiple indentations provides an average hardness and modulus over a range of crystallographic orientations. In this work, 5 to 8 different randomly-oriented crystals were selected for each growth condition, and 4-10 indentations were made per crystal, resulting in at least 28 measurements for each amino acid concentration.

Supplementary Note 1. Simulation protocols

The program Packmol[11] was used to place the amino acids inside the crystal in a random orientation for a range of 0-2.3 mol% (Asp^{1-}, Gly^{0}) or 0-3.2 mol% (Asp^{2-}, Gly^{1-}) of amino acid within the simulation box, corresponding to a maximum inclusion of 3.5, 3.9, 4.8 or 5.5 wt% for Asp^{1-}, Gly^{0}, Asp^{2-} and Gly^{1-} respectively. To avoid a net charge change in the system the solution chemistry shown in supplementary equations 1-4 was used. In all systems the calculations of the energetics of the excess Ca^{2+} and CO_3^{2-} ions were made with respect to bulk calcite such that our results did not depend on the reference state of the system.

$$Ca^{2+}(aq) + Asp^{2-}(aq) + Ca^{2+}(crystal) + [CO_3]^{2-}(crystal) => 2Ca^{2+}(aq) + 2[CO_3]^{2-}(aq) + Asp^{2-}(crystal) + V_{Ca}^{2-}(crystal) + 2V_{CO3}^{2+}(crystal) \quad \textit{(Supplementary Eq. 1)}$$

$$Ca^{2+}(aq) + 2Gly^{-}(aq) + Ca^{2+}(crystal) + [CO_3^{2-}](crystal) => 2Ca^{2+}(aq) + 2[CO_3]^{2-}(aq) + 2Gly^{-}(crystal) + V_{Ca}^{2-}(crystal) + 2V_{CO3}^{2+}(crystal) \quad \textit{(Supplementary Eq. 2)}$$

$$Ca^{2+}(aq) + 2Asp^{-}(aq) + Ca^{2+}(crystal) + [CO_3^{2-}](crystal) => 3Ca^{2+}(aq) + 3[CO_3]^{2-}(aq) + 2Asp^{-}(crystal) + 2V_{Ca}^{2-}(crystal) + 3V_{CO3}^{2+}(crystal) \quad \textit{(Supplementary Eq. 3)}$$

$$Gly(aq) + Ca^{2+}(crystal) + [CO_3^{2-}](crystal) => 2Ca^{2+}(aq) + 2[CO_3]^{2-}(aq) + Gly(crystal) + 2V_{Ca}^{2-}(crystal) + 2V_{CO3}^{2+}(crystal) \quad \textit{(Supplementary Eq. 4)}$$

where V_X^y means a vacancy of X with the effective charge given in the superscript y.

The atomic charges for the amino acids were calculated with AMBER Antechamber[12] using the AM1-BCC method[13]. This uses a semi-empirical method in combination with bond

charge corrections to calculate the electronic structure of the amino acid. For all simulations, the Molecular Dynamics package DL POLY Classic[14] was used and the mineral phase was described using the $CaCO_3$ potentials developed by Raiteri *et al*.[15] The interactions of the organic molecules were described using the AMBER forcefield[16]. The interactions between the mineral and organic phase were modelled by using a generic method to produce cross term potentials[17], where this generated a reliable potential for our system without the need for further fitting.

All simulations were run at a temperature of 300 K and at atmospheric pressure (10^5 Pa). The simulations were equilibrated for 100 ps using a timestep of 0.1 fs for an NVT ensemble with a Nosé-Hoover thermostat[18]. Subsequent simulations were carried out for data analysis. These simulations were run in an NPT ensemble with a timestep of 1.0 fs using a Nosé-Hoover thermostat and a Hoover barostat[19] for 2.0 ns. The insertion energy of the amino acids was calculated using the solution chemistry as described in Supplementary equation (1-4) above. In order to calculate the configuration energy of the system under anisotropic expansion, simulations with a configuration of 5 mM Asp^- were performed to mimic the experimental setup. The simulation box was expanded manually and independently along either the *c*-axis or the *a*-axis (the *b* axis is equivalent to a-axis) in increments of 0.05 % of the initial lattice parameter per step. After each expansion, the configurational energy was calculated during a 0.5 ps simulation with a 1.0 fs timestep in an NVT ensemble.

Supplementary Note 2. Derivation of equation (1) to describe the hardness of calcite crystals with occluded amino acids

Of the slip systems in calcite, $\{\bar{1}02\}\langle 2\bar{2}1\rangle^{+/-}$, $\{104\}\langle\bar{2}21\rangle^{+/-}$, and $\{\bar{1}08\}\langle 401\rangle^{+}$ have the lowest critical resolved shear stresses [20]. The $\{\bar{1}02\}$ and {104} systems have large Burgers

vectors and require high temperatures and/or pressures to operate, while the $\{\bar{1}08\}$ twinning system can be activated in uniaxial loading at room temperature and pressure[20]. Since at least 5 independent slip systems are needed for generalized plasticity, as required to form the indentations (Fig. 6a), it is evident that the pressure under the indenter is sufficient to activate the more difficult of these slip systems.

To determine the form of the relationship between H and F_c, we first estimate the dislocation line tension T from $T = \alpha G b^2$ where G is the shear modulus and b is the magnitude of the Burgers vector. Taking $\alpha = 1$, $G = 35$ GPa, and $b = 0.5$ nm (G and b calculated as averages for the material), we find $T \approx 9$ nN, which is significantly greater than the force required to break a covalent bond (estimated as 1.5 to 4 nN [21-23]), which in turn indicates that the angle θ at which the dislocation will cut the molecule will be low ($\leq 13^\circ$). Under these conditions, the critical resolved shear stress (τ_c) required for the dislocations cut the particles can be estimated from $\tau_c = (F_c / bL)\sqrt{F_c / 2T}$, where L is the average separation of the molecules in the lattice [24]. To convert τ_c to H, we use known critical resolved shear stresses for the slip systems in calcite [20] and our measured indentation modulus to estimate a yield stress (Y) to modulus (E) ratio of ≈ 0.01. Finite element simulations indicate that H approaches $2.8Y$ for materials with $Y/E < 0.02$[25]. Using this relationship, and the von Mises criterion to relate Y to τ_c, the hardness is related to the critical resolved shear stress by $H \approx 4.8\tau_c$. If we assume that strength of the crystal is just the sum of the intrinsic resistance to dislocation motion (as determined from the hardness, H_0, of pure Iceland spar) and the additional strengthening due to AA molecules, we can write the result as Equation 1.

$$H = H_0 + 4.8(F_c / bL)\sqrt{F_c / 2T} \qquad \text{(Equation 1)}$$

Supplementary Note 3. Estimation of lattice misfit of AA molecules in calcite

One distinction between solutes and second phase particles is their effect on lattice strains. A solute species has a certain size and replaces a fundamental unit of the host crystal that also has a certain size (or is inserted interstitially). Unless the solute and the space in the lattice into which it is inserted happen to be the same size and shape, accommodation strains are required *e.g.* when Mg^{2+} is substituted for Ca^{2+} in calcite[26-30]. In contrast, both a second phase particle and the space created for it in the crystal may consist of many formula units (atoms or molecules) which can be closely adjusted so that little or no lattice strains are required, *e.g.* ~ 200 nm polystyrene inclusions in calcite[31].

With respect to lattice distortions, amino acid inclusions behave like solutes. The closest fit for Gly^0 is achieved when it replaces one $CaCO_3$ formula unit, and the closest fit for Asp^{2-} when it replaces one $CaCO_3$ unit and one CO_3^{2-} ion. Using molecular volumes for Gly^0, $CaCO_3$, Asp^{2-}, and CO_3^{2-}, of 0.077 nm[332], 0.061 nm[333], 0.13 nm[334], and 0.055 nm^3 (found by subtracting the volume of a Ca^{2+} ion, i.e. 0.0056 nm[335], from that of $CaCO_3$), respectively, the misfit, expressed as $(r-r_0)/r_0$, where r and r_0 are the radii of spheres having the same volumes as the AA molecule and the space created for it in the lattice respectively, is 8.1% for Gly^0 and 3.9 % for Asp^{2-}. Similar calculations for $2Asp^{1-}$ and $2Gly^{1-}$ (as described in the simulations section) give misfits of 13.7 % and 9.9 %, respectively. It is noteworthy that not only do the strains from PXRD (Fig. 3) and simulations (Fig. 4) agree when Gly^0 and Asp^{2-} are considered as the occluding species, but the ratio of these strains is consistent with the ratio of the misfits, while any of the ratios including Gly^{1-} and Asp^{1-} are not. This suggests that the AA molecules are occluded as Gly^0 and Asp^{2-}, and not the paired molecules of Gly^{1-} and Asp^{1-} that were also considered in the simulations, in agreement with the NMR results.

These misfits result in large tensile strains in the calcite lattice in the neighborhood of each AA molecule, which drop off rapidly with distance from the molecule[36] (Fig. 3e). These distortions increase both the average lattice parameter (lattice distortions, Figs. 3a and 3b) and the inhomogeneity of the strains (microstrains, Figs. 3c and 3d and Supplementary Fig. 4). As $[AA]_{inc}$ increases, the strain fields around the molecules begin to overlap (note the small separation between molecules in Supplementary Fig. 9), and the strain inhomogeneity decreases as the lattice distortions continue to increase (Figs. 3e and 3f). Because the molecules are small and roughly equiaxed, the anisotropy in the lattice distortions (Figs. 3a and 3b) arises primarily from the elastic anisotropy of calcite (the stiffness along the *c* axis is 58% of that along the *a*-axis[37]).

Supplementary Note 4. Calculation of spacing, *L*, between amino acid molecules

As described in the main text, to determine the hardening mechanism of the amino acids, the spacing, *L*, between amino acid molecules within the calcite crystals must be determined. To calculate this value, we assume that the AA molecules are randomly distributed throughout the volume, consistent with the ssNMR data, and thus in any subset of that volume, such as a thin slice containing the slip plane. We convert the measured mole concentrations, $[AA]_{inc}$, to volume concentrations $C_{v,AA}$ (number of AA molecules/volume) using the known molecular volumes of calcite[33] and the amino acids in crystalline form[32,34] (there is very little difference between the polymorphs for our purposes). The number of AA molecules per unit area on the thin slice is then given by $C_{v,AA}*t$, where t is the thickness of the slice. Approximating the configuration of the molecules in the calcite as a square array, we have $L = (C_{v,AA}*t)^{-0.5}$. For

geometric consistency, we set t equal to the diameter D_{AA} of the AA molecule under consideration ($D_{AA} = \sqrt[3]{\frac{6v_{AA}}{\pi}}$, where v_{AA} is the volume of the amino acid), so

$$L = [C_{v,AA}]^{\frac{-1}{2}} \left[\frac{6v_{AA}}{\pi} \right]^{\frac{-1}{6}} . \qquad \text{(Supplementary Equation 5)}$$

A plot of L *vs.* $[AA]_{inc}$ is shown in Supplementary Fig. 9.

Supplementary Note 5. The possible role of twinning.

Twinning is a common deformation mechanism in bulk calcite. However, it requires specific loading and boundary conditions, which are not provided in our tests. Furthermore, if twinning does occur, the resulting hardening is still expected to follow a rule like Eq (1). These ideas can be understood as follows. Although the $\{\bar{1}08\}$ twin system in calcite has a lower critical resolved shear stress than the $\{\bar{1}02\}$ and {104} slip systems, formation of a $\{\bar{1}08\}$ twin requires enormous shear strains (69.4%)[38] and thus occurs only where accommodations can be made for incompatibilities between the twin and the surrounding material. Accordingly, reports of twin deformation occurring underneath indentations in calcite fall into two categories:

(1) Cases where the incompatibility is accommodated by cracking or the presence of a free surface or other interface. For example, Li and Ortiz found a great deal of twinning under indentations in *P. placenta*, due to the presence of many compliant interfaces that could accommodate the large twin shear displacements[39]. In their indentation tests of pure calcite, few twins formed and these spanned relatively short distances between free surfaces, including the sample surface and subsurface cracks.

(2) Cases where the shear required to accommodate the indenter is matched to the shear required by the twin. For example, 2-D wedge indentations have been used to study "elastic twinning"[38].

For indentations made with a Berkovich indenter, slip on the $\{\bar{1}08\}$ system has been seen, but only on the {001} face at azimuthal angles where the interaction between the geometry of the indenter and the orientation of the crystal, along with the free surface and the formation of cracks, allowed it[10].

We know of no study in which twins have been reported underneath indentations in single crystal calcite where no cracking (or other accommodating interface) was present. Furthermore, our experiments revealed no evidence of twinning in either the load-displacement data (*e.g.* "pop-in" events[39]) or in the surface profiles (Fig. 6a inset).

This discussion does not prove that twinning did not occur in our experiments. Even if there is twinning, however, twins grow by motion of "twin dislocations." These line defects can be more complicated than simple glide dislocations[40] but include a glide component that must interact with the occluded AA molecules. While new laws may be needed to account for temperature and rate dependence[41] the Friedel term in Eq 1 is geometric, and should apply equally well to full and twin dislocations in a comparative model such as ours (Eq. 1 compares the hardness of samples with and without occluded AA molecules subjected to identical tests). Thus, even if twinning occurs, we expect variations in hardness with AA content to follow Eq. 1 reasonably well.

a

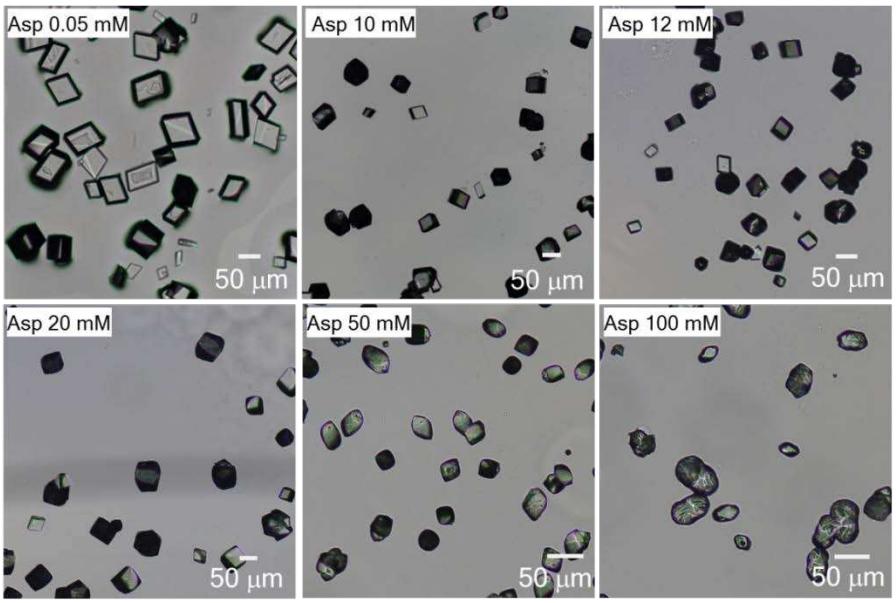

b

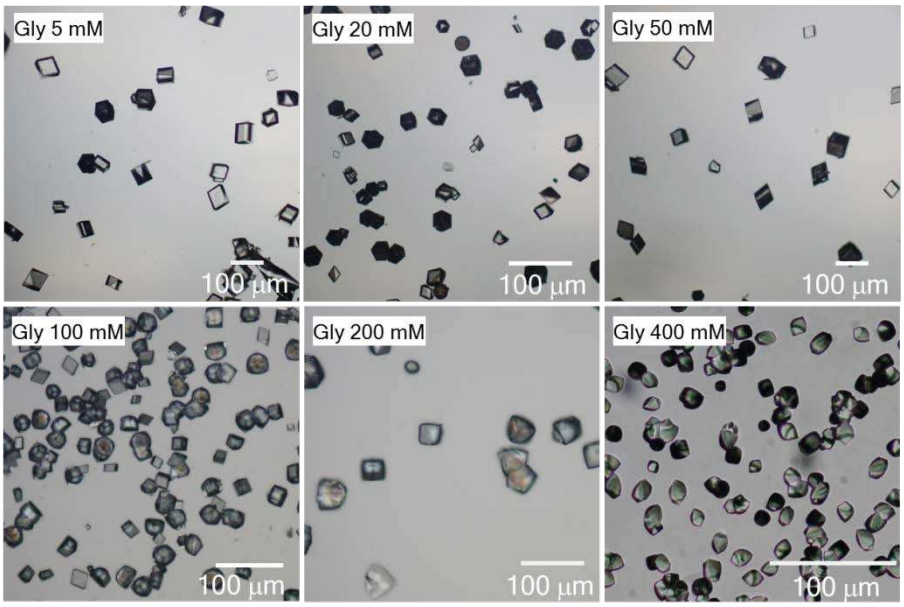

Supplementary Figure 1.

Optical microscope images of calcite crystals (a) showing morphological changes as a function of $[Asp]_{Sol}$ = 0.05 mM, 10 mM, 20 mM, 50 mM and 100 mM. (b) shows morphological change as a function of $[Gly]_{Sol}$ = 5 mM, 10 mM, 20 mM, 50 mM, 100 mM and 200 mM. All the crystals were grown at an initial $[Ca^{2+}]$ = 10 mM. Note that the scale bars are individual to each Figure and reflect the decrease in crystal size as the concentration of amino acid increases.

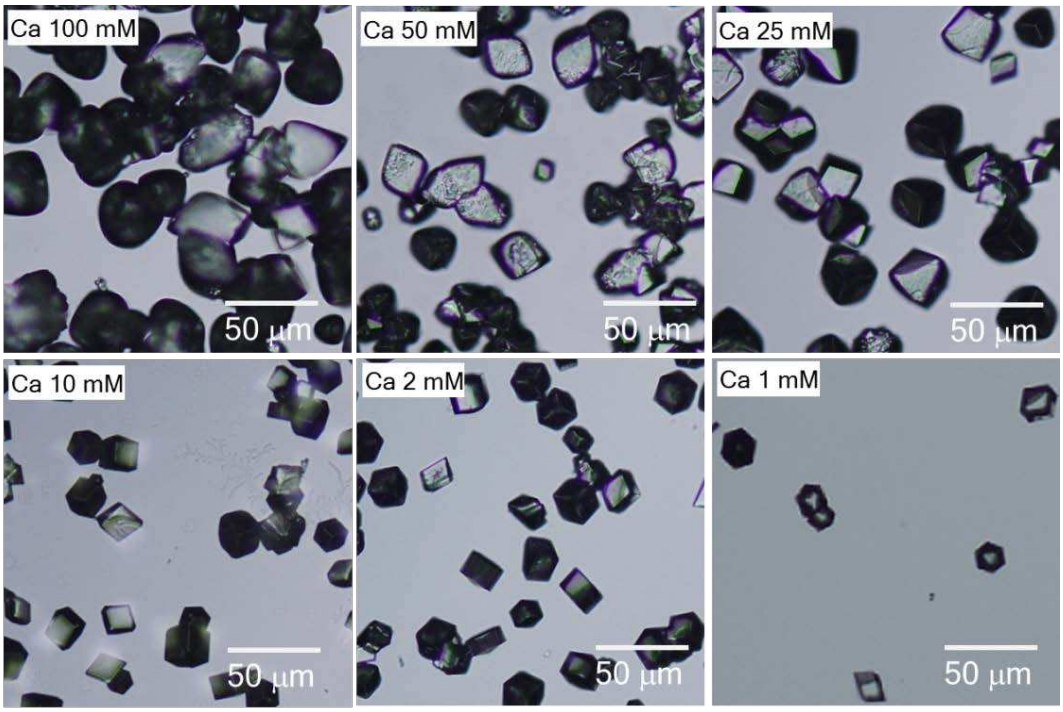

Supplementary Figure 2.

Optical microscope images of calcite crystals showing morphological changes as a function of the initial $[Ca^{2+}]$ = 100 mM, 50 mM, 25 mM, 10 mM, 2 mM and 1 mM. All of the crystals were grown in the presence of an initial $[Asp]_{sol}$ = 10 mM.

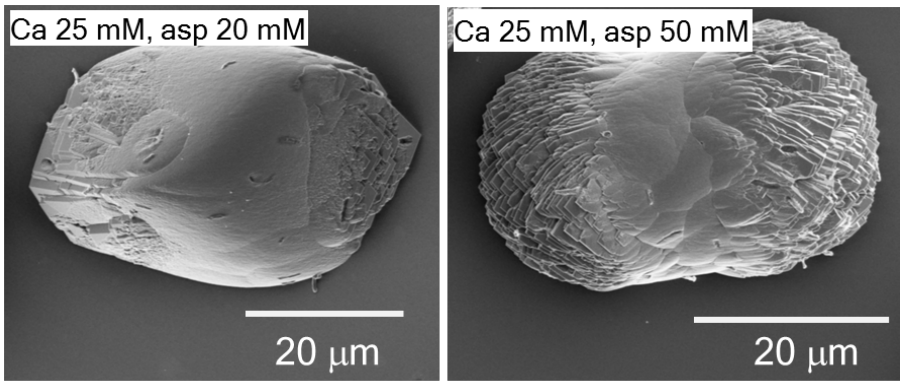

Supplementary Figure 3.

SEM images of calcite crystals grown at an initial $[Ca^{2+}]$ = 25 mM showing a modified single crystal morphology at $[Asp]_{sol}$ = 20 mM, and a polycrystalline particle at $[Asp]_{sol}$ = 20 mM.

a

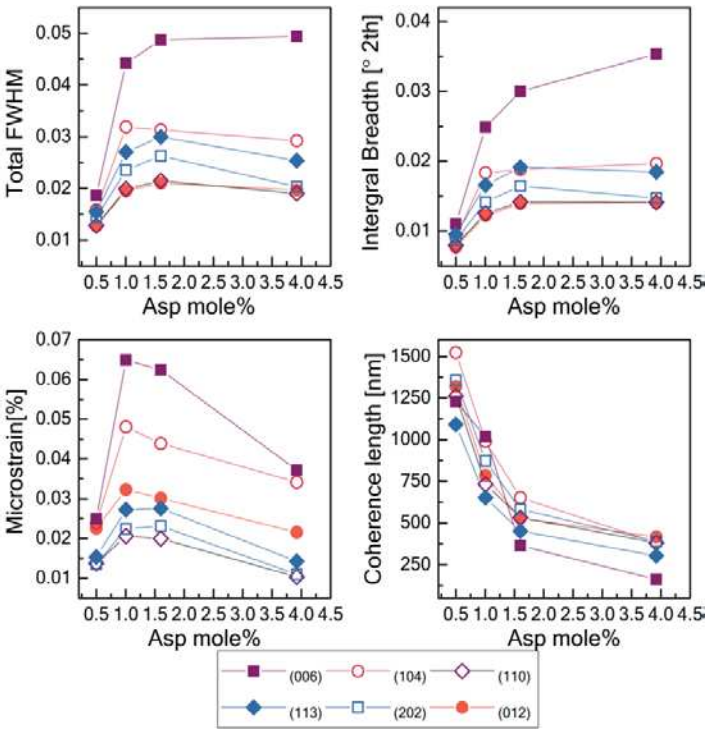

b

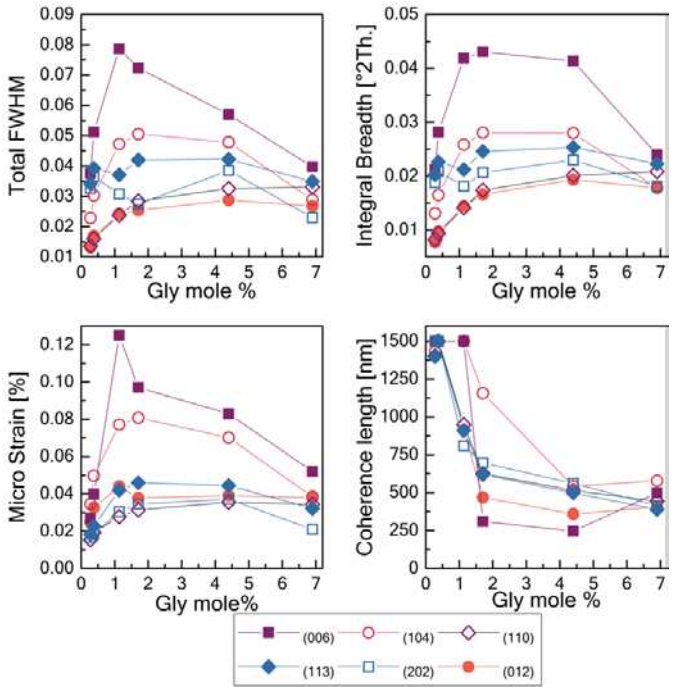

Supplementary Figure 4.

Changes in XRD peak Full Width at Half Maximum (FWHM), integral breadth, microstrain and coherence length induced by (a) Asp and (b) Gly incorporation.

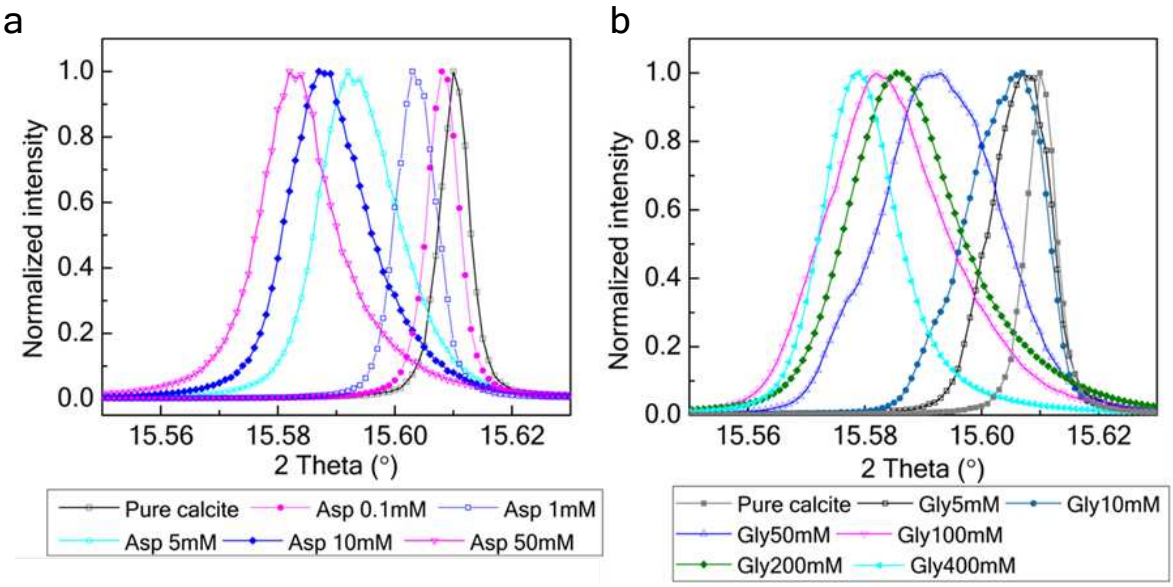

Supplementary Figure 5.

Changes in the positions and shapes of (104) reflections of the samples shown in Fig 3. The lattice shift and FWHM values of the peaks were shown in Fig 3. (A) The peaks shift to lower angles (higher d-spacings) with increasing occlusion of Asp, while at the same time increasing in width until [Asp] = 10 mM (1.67 mol %). The peak then becomes slightly more narrow at [Asp] = 50 mM. (B) The peaks shift to higher d-spacings with increased occlusion of Gly, while increasing in width until [Gly] = 50 mM, before narrowing again at higher values of [Gly].

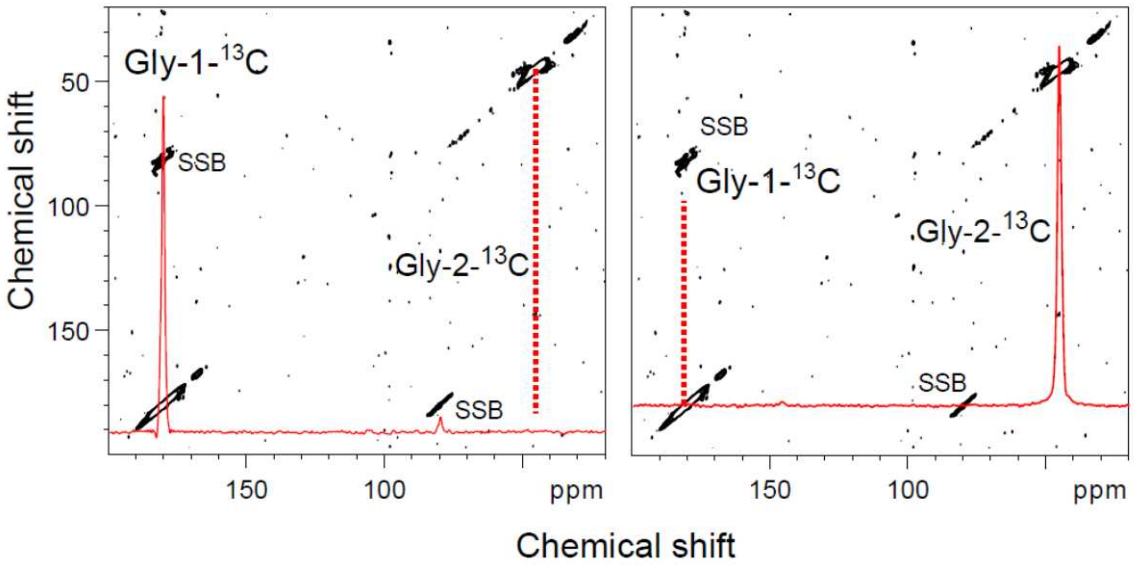

Supplementary Figure 6.

ssNMR showed no evidence for Gly-Gly intermolecular interactions or clustering. The black traces in each panel are (identical) contour plots of 2D proton driven spin diffusion (PDSD) data. The red traces depict rows extracted from the 2D plots at chemical shifts corresponding to the Gly-1C (left) and Gly-2C (right). If there were a detectable interaction between Gly neighbours we would see signals at the frequencies marked by dotted red lines in each trace, i.e. at the Gly-2C in the left panel, and Gly-1C in the right panel

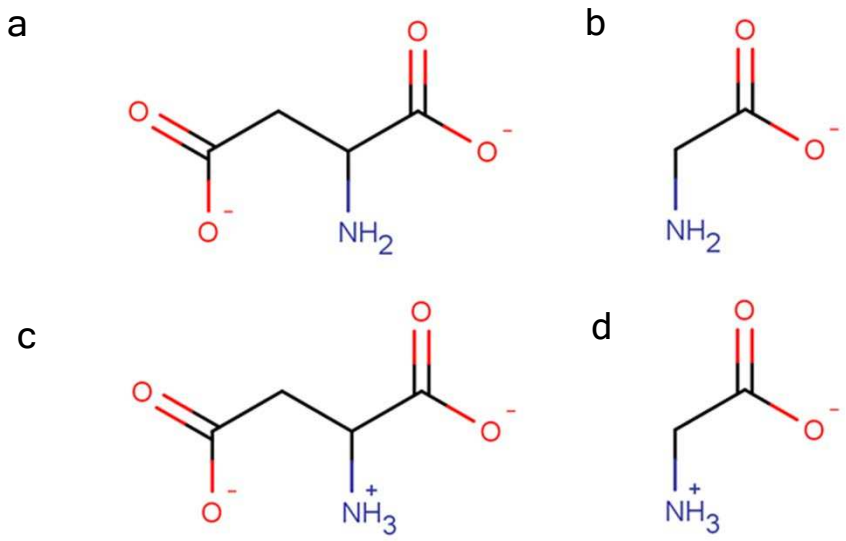

Supplementary Figure 7.

Chemical structures of the differently charged states of the aspartic acid and glycine used in simulations (a) Asp^{2-} (b) Gly^{1-} (c) Asp^{1-} (d) Gly^{0}.

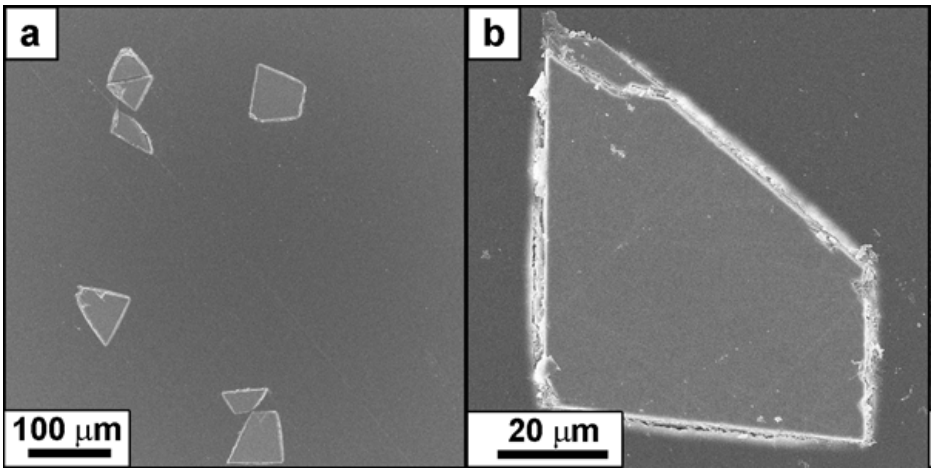

Supplementary Figure 8.

(a, b) Scanning electron micrographs of calcite crystals grown in the presence of [Asp] = 1 mM, embedded within cyanoacrylate resin, and polished to expose crystal surfaces for nanoindentation.

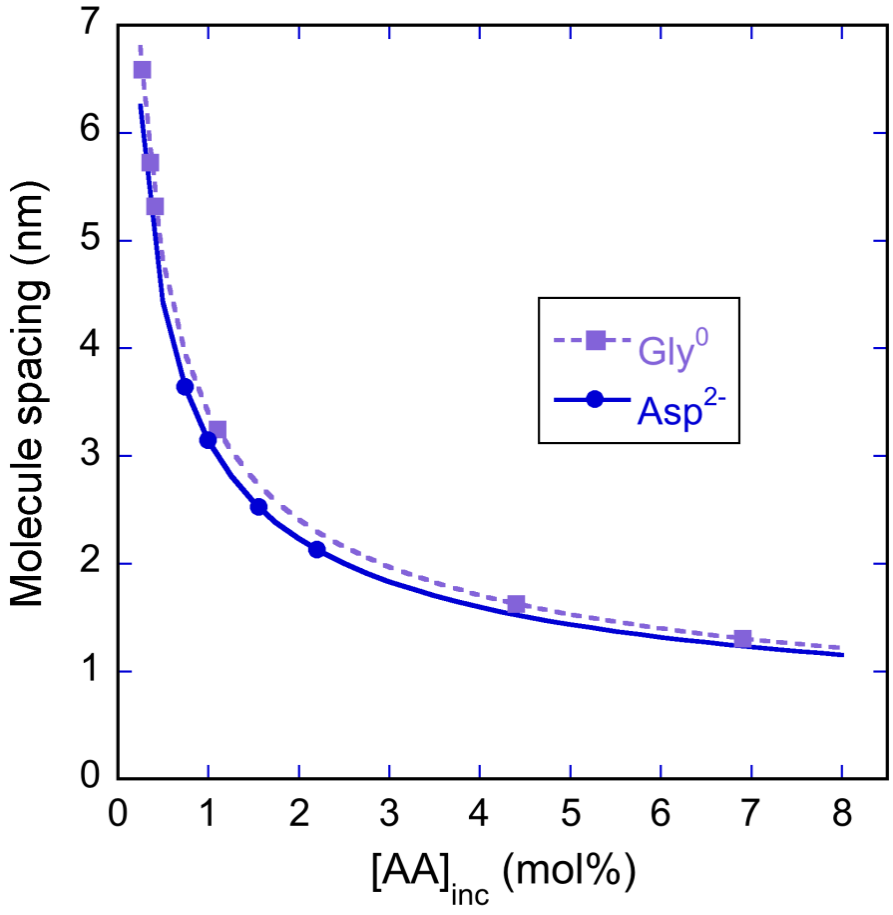

Supplementary Figure 9.

A plot showing intermolecular spacing, *vs.* $[AA]_{inc}$ calculated using Supplementary Equation 5. Symbols indicate the compositions of samples that were mechanically tested in this work.

Supplementary Table 1

XRD structure parameters and their goodness of fitness (GOF) of Asp/calcite and Gly/calcite shown in Fig. 3 as obtained from Rietveld analysis.

AA	conc [mM]	mol%	a(Å)	c(Å)	χ^2	$\Delta a/a$	$\Delta c/c$
Pure	0	0	4.9903	17.063	3.17	0	0
Asp	0.1	0.036	4.9907	17.068	6.355	8.02E-05	2.93E-04
Asp	1	0.5	4.9915	17.076	3.454	2.40E-04	7.62E-04
Asp	5	1.006	4.9921	17.096	18	3.61E-04	1.93E-03
Asp	10	1.673	4.9923	17.105	10.3	4.01E-04	2.46E-03
Asp	50	3.992	4.9927	17.114	11.30	4.81E-04	2.99E-03
Asp	100	2.728	4.9916	17.110	5.71	2.61E-04	2.75E-03
Gly	5	0.28	4.9907	17.069	11.38	8.02E-05	3.52E-04
Gly	10	0.387	4.9908	17.073	26.89	1.00E-04	5.86E-04
Gly	50	1.138	4.9918	17.102	29.85	3.01E-04	2.29E-03
Gly	100	1.707	4.9931	17.120	22.79	5.61E-04	3.34E-03
Gly	200	4.4	4.9931	17.136	15.27	5.53E-04	4.31E-03
Gly	400	6.9	4.9936	17.152	14.36	6.59E-04	5.24E-03

Supplementary Table 2

Goodness of Fitness values obtained from line profile analysis of Asp/calcite and Gly/calcite samples shown in Fig. 3. (a) Asp/calcite samples (b) Gly/calcite samples.

a

Reflection	Asp 1 mM	Asp 10 mM	Asp 5 mM	Asp 50 mM	Asp 100 mM
(012)	1.01	1.87	1.64	0.98	3.00
(104)	4.00	4.56	5.23	3.98	3.82
(006)	0.84	1.05	1.26	0.78	0.78
(110)	1.23	1.48	3.13	0.94	1.13
(113)	1.53	2.40	2.68	1.40	1.43
(202)	1.60	1.47	3.14	1.30	1.21

b

Reflection	Gly 5 mM	Gly 10 mM	Gly 50 mM	Gly 100 mM	Gly 200 mM	Gly 400 mM
(012)	1.19	2.26	1.26	1.05	2.87	2.35
(104)	7.33	7.43	3.88	4.72	11.78	12.18
(006)	0.82	2.11	0.95	0.97	1.56	1.42
(110)	1.42	2.45	2.33	1.96	3.73	2.50
(113)	1.74	1.32	2.48	3.61	5.10	3.32
(202)	0.88	1.39	1.34	5.30	3.57	7.73

Supplementary References

1 Ihli, J., Bots, P., Kulak, A., Benning, L. G. & Meldrum, F. C. Elucidating mechanisms of diffusion-based calcium carbonate synthesis leads to controlled mesocrystal formation. *Adv. Funct. Mater.* **23**, 1965-1973 (2013).

2 Penkman, K. E. H., Kaufman, D. S., Maddy, D. & Collins, M. J. Closed-system behaviour of the intra-crystalline fraction of amino acids in mollusc shells. *Quat. Geochronol* **3**, 2-25 (2008).

3 Demarchi, B. *et al.* Intra-crystalline protein diagenesis (IcPD) in Patella vulgata. part I: isolation and testing of the closed system. *Quat Geochronol* **16**, 144-157 (2013).

4 Tomiak, P. J. *et al.* Testing the limitations of artificial protein degradation kinetics using known-age massive Porites coral skeletons. *Quat Geochronol* **16**, 87-109 (2013).

5 Kaufman, D. S. & Manley, W. F. A new procedure for determining DL amino acid ratios in fossils using reverse phase liquid chromatography. *Quat. Sci. Rev.* **17**, 987-1000 (1998).

6 Demarchi, B. *et al.* New Experimental Evidence for In-Chain Amino Acid Racemization of Serine in a Model Peptide. *Anal. Chem.* **85**, 5835-5842 (2013).

7 Szeverenyi, N. M., Sullivan, M. J. & Maciel, G. E. Observation of spin Exchange by two-dimensional fourier-transform C-13 cross polarization-magic-angle spinning. *J. Magn. Reson.* **47**, 462-475 (1982).

8 Thompson, S. P. *et al.* Beamline I11 at Diamond: a new instrument for high resolution powder diffraction. *Rev. Sci. Instrum.* **80**, 075107 (2009).

9 Oliver, W. C. & Pharr, G. M. Measurement of hardness and elastic modulus by instrumented indentation: advances in understanding and refinements to methodology. *J. Mater. Res.* **19**, 3-20 (2004).

10 Kunitake, M. E., Mangano, L. M., Peloquin, J. M., Baker, S. P. & Estroff, L. A. Evaluation of strengthening mechanisms in calcite single crystals from mollusk shells. *Acta Biomater.* **9**, 5353-5359 (2013).

11 Martinez, L., Andrade, R., Birgin, E. G. & Martinez, J. M. PACKMOL: A package for building initial configurations for molecular dynamics simulations. *J. Comput. Chem.* **30**, 2157-2164 (2009).

12 Wang, J. M., Wang, W., Kollman, P. A. & Case, D. A. Automatic atom type and bond type perception in molecular mechanical calculations. *J. Mol. Graphics Modell.* **25**, 247-260 (2006).

13 Jakalian, A., Jack, D. B. & Bayly, C. I. Fast, efficient generation of high-quality atomic charges. AM1-BCC model: II. parameterization and validation. *J. Comput. Chem.* **23**, 1623-1641 (2002).

14 Todorov, I. T., Smith, W., Trachenko, K. & Dove, M. T. DL_POLY_3: new dimensions in molecular dynamics simulations via massive parallelism. *J. Mater. Chem.* **16**, 1911-1918 (2006).

15 Raiteri, P., Gale, J. D., Quigley, D. & Rodger, P. M. Derivation of an accurate force-field for simulating the growth of calcium carbonate from aqueous solution: a new model for the calcite-water interface. *J. Phys. Chem. C* **114**, 5997-6010 (2010).

16 Wang, J. M., Wolf, R. M., Caldwell, J. W., Kollman, P. A. & Case, D. A. Development and testing of a general amber force field. *J. Comput. Chem.* **25**, 1157-1174 (2004).

17 Freeman, C. L. *et al.* New forcefields for modeling biomineralization processes. *J. Phys. Chem. C* **111**, 11943-11951 (2007).

18 Hoover, W. G. Canonical dynamics - equilibrium phase-space distributions. *Phys. Rev. A* **31**, 1695-1697 (1985).
19 Melchionna, S., Ciccotti, G. & Holian, B. L. Hoover npt dynamics for systems varying in shape and size. *Mol. Phys.* **78**, 533-544 (1993).
20 DeBresser, J. H. P. & Spiers, C. J. Strength characteristics of the r, f, and c slip systems in calcite. *TCTOAM* **272**, 1-23 (1997).
21 Akbulatov, S., Tian, Y. C. & Boulatov, R. Force-reactivity property of a single monomer is sufficient to predict the micromechanical behavior of its polymer. *J. Am. Chem. Soc.* **134**, 7620-7623 (2012).
22 Diesendruck, C. E. *et al.* Mechanically triggered heterolytic unzipping of a low-ceiling-temperature polymer. *Nat. Chem.* **6**, 624-629 (2014).
23 Grandbois, M., Beyer, M., Rief, M., Clausen-Schaumann, H. & Gaub, H. E. How strong is a covalent bond? *Science* **283**, 1727-1730 (1999).
24 Friedel, J. *Les Dislocations*. 72 (Gauthier-Villars, Paris, 1956).
25 Cheng, Y. T. & Cheng, C. M. Scaling approach to conical indentation in elastic-plastic solids with work hardening. *J. Appl. Phys.* **84**, 1284-1291 (1998).
26 Kunitake, M. E., Baker, S. P. & Estroff, L. A. The effect of magnesium substitution on the hardness of synthetic and biogenic calcite. *MRS Commun.* **2**, 113-116 (2012).
27 Moureaux, C. *et al.* Structure, composition and mechanical relations to function in sea urchin spine. *J. Struct. Biol.* **170**, 41-49 (2010).
28 Perez-Huerta, A., Cusack, M., Zhu, W. Z., England, J. & Hughes, J. Material properties of brachiopod shell ultrastructure by nanoindentation. *J. R. Soc., Interface* **4**, 33-39 (2007).
29 Griesshaber, E. *et al.* Crystallographic texture and microstructure of terebratulide brachiopod shell calcite: an optimized materials design with hierarchical architecture. *Am. Mineral.* **92**, 722-734 (2007).
30 Wang, R. Z., Addadi, L. & Weiner, S. Design strategies of sea urchin teeth: structure, composition and micromechanical relations to function. *Philos. Trans. R. Soc., B* **352**, 469-480 (1997).
31 Kim, Y. Y. *et al.* Bio-inspired synthesis and mechanical properties of calcite-polymer particle composites. *Adv. Mater.* **22**, 2082-2086 (2010).
32 Perlovich, G. L., Hansen, L. K. & Bauer-Brandl, A. The polymorphism of glycine - Thermochemical and structural aspects. *J. Therm. Anal. Calorim.* **66**, 699-715 (2001).
33 Anthony, J. W., Bideaux, R. A., Bladh, K. W. & Nichols, M. C. in *Handbook of Mineralogy* Ch. V (Borates, Carbonates, Sulfates), (Mineralogical Society of America, ed. 2003).
34 Bendeif, E. E. & Jelsch, C. The experimental library multipolar atom model refinement of L-aspartic acid. *Acta Crystallogr., Sect. C: Cryst. Struct. Commun.* **63**, O361-O364 (2007).
35 Shannon, R. Revised effective ionic radii and systematic studies of interatomic distances in halides and chalcogenides. *Acta Crystallogr., Sect. A: Found. Adv.* **32**, 751-767 (1976).
36 Eshelby, J. D. The determination of the elastic field of an ellipsoidal inclusion, and related problems. *Proc. R. Soc. London, Ser. A* **241**, 376-396 (1957).
37 Bass, J. D. in *Mineral Physics & Crystallography: A Handbook of Physical Constants* 45-63 (American Geophysical Union, 2013).
38 Clayton, J. D. & Knap, J. Phase field modeling of twinning in indentation of transparent crystals. *Modell. Simul. Mater. Sci. Eng.* **19**, 085005 (2011).

39 Li, L. & Ortiz, C. Pervasive nanoscale deformation twinning as a catalyst for efficient energy dissipation in a bioceramic armour. *Nat. Mater.* **13**, 501-507 (2014).
40 Mullner, P. Between microscopic and mesoscopic descriptions of twin-twin interaction. *Z Metallkd* **97**, 205-216 (2006).
41 Ghazisaeidi, M., Hector, L. G. & Curtin, W. A. Solute strengthening of twinning dislocations in Mg alloys. *Acta Mater.* **80**, 278-287 (2014).